Enhanced Crop Discrimination and Monitoring Using Compact-Polarimetric SAR Signature Analysis From RADARSAT Constellation Mission

Hamid Jafarzadeh, *Graduate Student Member, IEEE*, Abhinav Verma, *Graduate Student Member, IEEE*, Masoud Mahdianpari, *Senior Member, IEEE*, Avik Bhattacharya, *Senior Member, IEEE*, and Saeid Homayouni, *Senior Member, IEEE*

***Abstract*—With the rapid advancements in SAR systems aiming for operational capabilities, crop characterization using compact-polarimetric synthetic aperture radar (CP-SAR) data has gained considerable attention. This study thoroughly assesses the potential usefulness of C-band SAR data in CP mode using the RADARSAT Constellation Mission (RCM) for crop monitoring. The research unfolds across two separate phases: 1) Extensive crop scattering characterization and 2) Crop classification. In the first part, we introduce three descriptors: compact-polarimetric SAR signature (CPS), differential CPS (DCPS), and the geodesic distance (GD) between signatures, to characterize the scattering pattern of four crop types: soybean, hay, corn, and cereal. We, then, derive the μ parameter and employ it in the $\mu - \chi$ decomposition method. Time-series investigation of the proposed descriptors and the three power components: P_s, P_d, and P_v provide valuable insights into the scattering responses exhibited by crops, facilitating a robust assessment and tracking of their growing cycle, thus, enabling the potential for improving crop discrimination. In the second part, we employ the $\mu - \chi$ and $m - \chi$ decompositions and wave descriptors to extract a stack of CP features for crop mapping. Combining diverse feature types and leveraging single- and multi-date RCM images, classification experiments yield an optimal classification map with an overall accuracy of 89.71%, particularly when utilizing features extracted from multi-date datasets. This study illustrates a substantial effort in crop classification, underscoring the potential of the RCM CP-SAR mission. Furthermore, our findings emphasize the potential of CP-SAR data from the RCM mission in contributing to precision agriculture and sustainable crop management practices.**

***Index Terms*—Agriculture, compact polarimetry (CP), decomposition, RADARSAT Constellation Mission (RCM), synthetic aperture radar (SAR).**

Manuscript received 11 September 2023; revised 10 December 2023 and 18 January 2024; accepted 9 February 2024. Date of publication 19 February 2024; date of current version 13 March 2024. This work was supported in part by the 2020–2022 Quebec-Maharashtra Cooperation Program of the Quebec Ministry of International Relations and Francophonie. *(Corresponding author: Hamid Jafarzadeh.)*

Hamid Jafarzadeh is with the Department of Electrical and Computer Engineering, Memorial University of Newfoundland, St. John's, NL A1B 3X5, Canada (e-mail: hjafarzadeh@mun.ca).

Abhinav Verma and Avik Bhattacharya are with the Microwave Remote Sensing Lab, Centre of Studies in Resources Engineering, IIT Bombay, Mumbai 400076, India (e-mail: averma.iirs@gmail.com; avikb@csre.iitb.ac.in).

Masoud Mahdianpari is with the Department of Electrical and Computer Engineering, Memorial University of Newfoundland, St. John's, NL A1B 3X5, Canada, and also with C-CORE, St. John's, NL A1B 3X5, Canada (e-mail: m.mahdianpari@mun.ca).

Saeid Homayouni is with the Centre Eau Terre Environnement, Institut National de la Recherche Scientifique, Québec City, QC G1K 9A9, Canada (e-mail: saeid.homayouni@inrs.ca).

Digital Object Identifier 10.1109/JSTARS.2024.3366883

I. Introduction

THE introduction is organized into four sections. The first three sections delve into comprehensive reviews of crop mapping and characterization studies. They underscore the overarching importance and utility of data derived from the RADARSAT Constellation Mission (RCM) Compact-Polarimetric Synthetic Aperture Radar (CP-SAR), providing insights into existing research endeavors dedicated to crop classification using CP-SAR data. The fourth section succinctly outlines the specific research objectives guiding this work.

A. Crop Mapping and Characterization

Crop mapping is one of the most traditional applications of Earth observation (EO) in agriculture from both onboard spaceborne and airborne platforms [1]. Crop mapping and inventory serve as the foundation for numerous environmental and socio-economic applications [2], [3], including supply chain management, crop insurance, yearly cropping patterns change delineation, and crop production estimation [4], [5], [6], [7]. Thus, providing accurate and reliable information about crops and their acreage is particularly interesting to scientific and operational applications and always presents a significant challenge.

Satellite EO, either passive or active, can provide timely and reliable information on crop conditions over vast areas, with high revisit frequency and high resolution [8], [9]. Over the past decades, remote sensing has made significant advancements in identifying and monitoring crop growth, phenology, and other biophysical parameters, though several issues remain to be resolved. As such, the use of EO for sustainable agricultural management and food security, and gathering farming information, such as crop growth assessment and crop acreage estimation, has become quite common [10], [11], [12].

Given the advent of new space instruments and rapid progress of techniques for land cover discrimination, crop types can be classified more accurately using EO techniques that observe the land surface at wavelengths ranging from visible/near-infrared

to microwave. With the help of data analytics, either seasonally stable (e.g., soil type and land cover) or variable (e.g., weed or insect infestation, crop stress, crop disease, crop yield, and soil moisture) parameters can be mapped during the agricultural growing season. Thanks to remote sensing imagery, a wide variety of space-based sources of information are now available, empowering crop monitoring to be carried out on broader scales [2]. As such, significant efforts have been made in the remote sensing community to adequately utilize these sources for crop characterization and classification throughout various studies [13], [14], [15], [16].

B. RCM CP-SAR Data

Owing to its weather-, illumination-, and time-independent characteristics, SAR data has been extensively used in the context of crop type identification [17], [18], yield estimation [19], [20], and biophysical parameter calculation [21], [22], as well as vegetation indices formulation [23]. SAR components, particularly the acquisition wavelength, polarization, and incidence angle, strongly affect the reflected signals from the target [6], [24]. As a result, the collected backscattering SAR signals influenced by vegetation and soil properties carry information related to crop and soil's geometric structure and dielectric properties [12], [25].

In particular, the RCM imagery offers great crop characterization and mapping opportunities. The RCM was designed as the next generation of the Canadian RADARSAT program, following the highly successful RADARSAT-1 and RADARSAT-2 missions. This constellation configuration comprised three identical C-band SAR satellites launched in the summer of 2019 into closely coordinated orbits, providing a four-day repeat cycle [26], [27]. With RCM datasets, the potential of CP emerged as a viable mode to address the needs of users seeking wide swath coverage while preserving polarization richness [28].

The RCM CP-SAR architecture transmits a circularly polarized signal and coherently records both the horizontal and vertical components (H + V) of the backscattered signal, i.e., the circular-transmit and linear-receive (CL) configuration [27]. This configuration is achieved by simultaneously driving the H and V feeds with a 90° phase difference [28]. By utilizing a single transmit polarization, the power requirements are significantly reduced compared with full polarimetric (FP) modes [29].

C. Review of CP Research for Crop Classification

Studies using simulated CP-SAR data have demonstrated the potential of the CP acquisition mode described by [28] in providing valuable sets of applications, such as wetland classification maps [30] and accurate crop inventories [29], [31]. Many published studies have simulated CP data from the FP acquisition mode due to limited access to CP data, as most studies have utilized FP data from RADARSAT-2 to accomplish several applications.

For instance, Charbonneau et al. [31] studied the potential of the CP mode for agricultural crop classification. The study used four RADARSAT-2 images captured during the growing season over the Agriculture and Agri-Food Canada (AAFC) over the eastern Ontario region to generate and simulate CP datasets. With the decision tree classifier applied to the multitemporal Stokes vector parameters, end-of-season crop mapping produced high accuracy. Further, Stokes parameters from CP data generated superior accuracy for early-season crop mapping than dual-polarization (DP) and the Freeman–Durden decomposition parameters. This study serves as a promising early indication of the circular polarization's (CP) potential for crop classification within the agriculture community.

Brisco et al. [32] evaluated DP, FP, and simulated CP-SAR data derived from four RADARSAT-2 images acquired over a study site in China for rice mapping and performed classification using the support vector machine classifier. The study revealed that simulated CP data outperformed DP data, although it did not reach the same level of accuracy as FP data. However, the authors stated that the classification accuracy increases as one goes up the polarization hierarchy. Xie et al. [33] conducted a similar study to analyze DP, FP, and simulated CP-SAR data response for different crop types for a test study in the Leizhou Peninsula, southern China. The experiments were conducted on time-series images acquired by X-band TerraSAR-X. The classification results revealed a slight difference in the accuracy of the simulated CP data with other acquisition modes. Using four RADARSAT-2 images, Mahdianpari et al. [26] investigated the effect of polarization difference between FP data. They simulated CP-SAR data with a focus on mapping mid-season crop productions in an agricultural region in Manitoba, Canada. As outlined in their study, the CP-SAR data demonstrated higher accuracy compared with DP data but fell short of the accuracy achieved with FP data when classifying crop types using the random forest (RF) classifier.

In a recent study, Robertson et al. [29] used 17 RCM images acquired in CP mode for crop monitoring. They used the Stokes and $m - \chi$ decomposition parameters within the RF classifier. They asserted that examining scattering responses on the Poincaré sphere unveils polarization changes corresponding to crop phenology. This approach enhances the differentiation of crop types, particularly during dynamic growth stages such as mid-season.

Some studies have also reported the sensitivity of CP parameters toward agricultural crop characteristics. Kumar et al. [34] noted that the growth patterns of wheat and corn significantly impact CP parameters. In addition, Ballester-Berman and Lopez-Sanchez [35] examined the time series of CP parameters across crops, revealing multiple correlations between these parameters and agricultural biophysical factors.

D. Research Objectives

Polarimetric decomposition is a vital technique for extracting meaningful polarimetric parameters from SAR data, providing insights into the physical characteristics of natural surfaces and aiding in land cover mapping. As SAR technology advances, especially with the advent of regional coverage and high-resolution data offered by RCM, innovative methodologies for crop monitoring have become increasingly relevant. This research focuses on evaluating the significance of RCM CP-SAR data in crop monitoring and characterization.

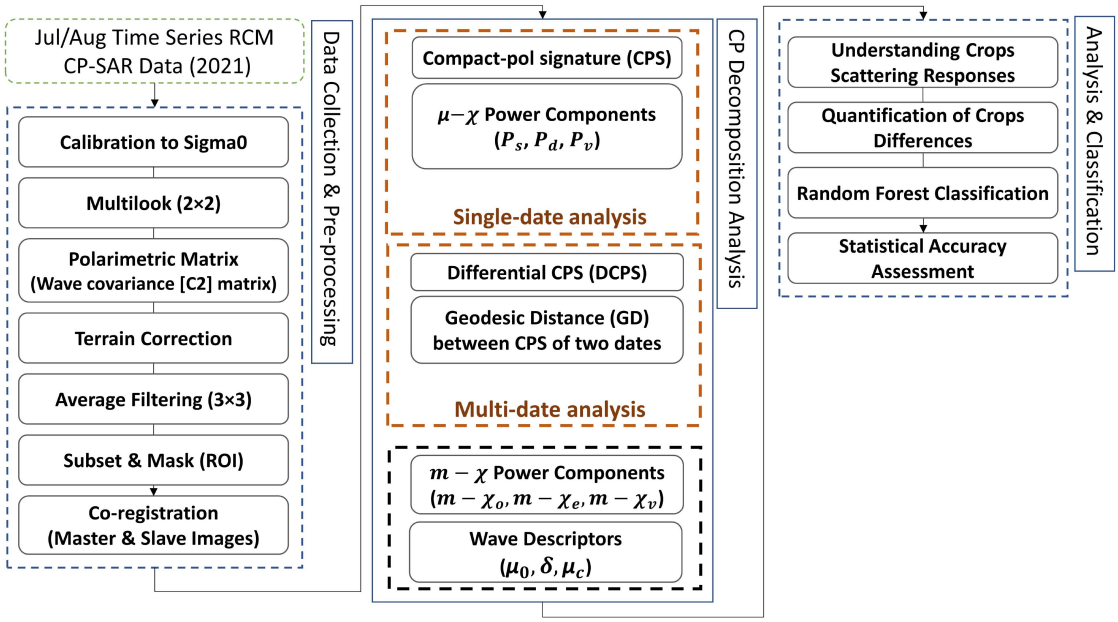

Fig. 1. Processing flow diagram of the study with the focus on single-date and multi-date analysis of CP-SAR features for crop characterization.

The primary objective of this study is to explore the utility of the recently introduced compact-polarimetric signature (CPS) and assess its potential in enhancing crop monitoring using RCM data. In addition, a secondary scientific objective aims to expand the CPS concept by introducing novel descriptors, namely, differential CPS (DCPS) and geodesic distance (GD) between CPSs. Furthermore, a new decomposition technique is introduced, and classification scenarios are designed based on the decomposition parameters derived from a temporal stack of CP features. The implications of this analysis with RCM imagery extend not only to Canadian agricultural operations but also hold promise for enhancing agricultural monitoring activities on a regional and national scale.

The rest of this article is organized as follows. Section II outlines the methodology for retrieving CPS, DCPS, GD, and $\mu - \chi$ decomposition powers using time-series RCM CP-SAR data. An overview of the study area and the data sources is provided in Section III. Section IV presents the analysis of the time-series results, emphasizing the importance of the proposed methodology. Finally, Section V concludes this article.

II. Methodology and Experimental Design

In this section, we present the formulation of the CPS, DCPS, and GD between two CPSs. In addition, we introduce a parameter μ derived from the CPS to formulate the $\mu - \chi$ decomposition. The overall stages of the proposed methodology are illustrated in Fig. 1.

A. Compact-Polarimetric SAR Signature (CPS)

CP-SAR systems transmit a circularly polarized wave, either left-handed (L) or right-handed (R) circular, and coherently receive the linear horizontal (H) and vertical (V) polarized components of the scattered wave. Following calibration and processing, the scattered wave information can be represented in terms of a 2×1 element complex Jones vector, denoted as $\vec{E}$, for each pixel in the image for any arbitrary transmit wave. Note that, in CP mode, we only measure a projection of the 2×2 complex scattering matrix $\mathbf{S}$ as [36]

$$\vec{E} = \begin{bmatrix} E_{CH} \\ E_{CV} \end{bmatrix} = \frac{1}{\sqrt{2}} \begin{bmatrix} S_{HH} & S_{HV} \\ S_{VH} & S_{VV} \end{bmatrix} \begin{bmatrix} 1 \\ \pm i \end{bmatrix} = \frac{1}{\sqrt{2}} \begin{bmatrix} S_{HH} \pm iS_{HV} \\ S_{VH} \pm iS_{VV} \end{bmatrix} \tag{1}$$

where the subscript C represents the polarization of the transmitted wave (L: left-handed or R: right-handed circular transmit) and H and V represent the linear horizontal and vertical polarization of the received wave. Note that the $+$ sign is for L circular transmit, and $-$ is for R circular transmit. As mentioned above, the RCM data is acquired using R circular polarization mode, thus, corresponding to a $-$ sign for the subscript C.

Therefore, utilizing the elements of the complex Jones vector $\vec{E}$, the 2×2 covariance matrix $\mathbf{C_2}$ can be derived as

$$\mathbf{C_2} = \begin{bmatrix} \langle |E_{CH}|^2 \rangle & \langle E_{CH} E_{CV}^* \rangle \\ \langle E_{CV} E_{CH}^* \rangle & \langle |E_{CV}|^2 \rangle \end{bmatrix} = \begin{bmatrix} C_{11} & C_{12} \\ C_{21} & C_{22} \end{bmatrix}. \tag{2}$$

With CP-SAR data, the elements of the $\mathbf{C_2}$ can be used to compute the 4×1 Stokes vector of the scattered wave as

$$\boldsymbol{g_s} = \begin{bmatrix} g_0 \\ g_1 \\ g_2 \\ g_3 \end{bmatrix} = \begin{bmatrix} \langle |E_{CH}|^2 + |E_{CV}|^2 \rangle \\ \langle |E_{CH}|^2 - |E_{CV}|^2 \rangle \\ 2\Re \langle E_{CH} E_{CV}^* \rangle \\ 2\Im \langle E_{CH} E_{CV}^* \rangle \end{bmatrix} = \begin{bmatrix} C_{11} + C_{22} \\ C_{11} - C_{22} \\ 2\Re\, C_{12} \\ 2\Im\, C_{12} \end{bmatrix}. \tag{3}$$

The polarization structure of the scattered wave is determined by two wave parameters: The "ellipticity angle" (χ) and the "orientation angle" (ψ). One can describe the polarization state of the scattered wave using the Stokes vector, $\boldsymbol{g_s}$. It should be noted that the transmit and receive antenna's polarization basis are both synthesized for $-45^\circ \leq \chi_{t,r} \leq 45^\circ$, and $-90^\circ \leq \psi_{t,r} \leq 90^\circ$ in the full-polarimetric signature (FPS). Hence, in FPS, one measures the power received when the receiving antenna's polarization aligns with that of the transmitting antenna (co-pol signature) and when the polarization of the transmitting antenna is orthogonal to that of the receiving antenna (cross-pol signature) [37].

In contrast to the FP mode, the CP mode maintains a constant transmit antenna polarization (i.e., either L or R). Hence, in this mode, we only synthesize the receive antenna's polarization state ($-45^\circ \leq \chi_r \leq 45^\circ$ and $-90^\circ \leq \psi_r \leq 90^\circ$). Consequently, Verma et al. [38], [39] extended the concept of polarization signature from FP-SAR data to DP- and CP-SAR data. Thus, once the Stokes vector is determined, the received power of CP-SAR mode can be synthesized for any receive antenna polarization basis. This capability enhances the versatility of CP-SAR systems, enabling a detailed exploration of polarimetric signatures under varying receive antenna polarization basis as

$$\begin{aligned} P_{\text{CP}}(\chi_r, \psi_r) &= \boldsymbol{g_r}^T \mathbf{K}\, \boldsymbol{g_t} \\ &= \boldsymbol{g_r}^T \boldsymbol{g_s} \\ &= \begin{bmatrix} 1 \\ \cos 2\chi_r \cos 2\psi_r \\ \cos 2\chi_r \sin 2\psi_r \\ \sin 2\chi_r \end{bmatrix}^T \boldsymbol{g_s} \end{aligned} \tag{4}$$

where the Stokes vector $\boldsymbol{g_s} = \mathbf{K}\, \boldsymbol{g_t}$ describes the polarization state of the scattered wave, and the superscript T denotes the vector transpose. The Stokes vectors $\boldsymbol{g_t}$, and $\boldsymbol{g_r}$ describe the polarization state of the transmit and receive antennas, respectively. We, then, represent the synthesized received power, P_{CP} (91×181), using a 2-D plot. For visualization, we display the χ and ψ along the x- and y-axis of the CPS. The magnitude of the synthesized received power, obtained by varying the polarization state of the receiving antenna, is presented using a color bar for enhanced interpretation.

B. Differential Compact-Polarimetric Signature (DCPS)

The DCPS descriptor serves as a powerful tool for investigating dynamic changes in scattering from targets over different observation dates for all χ_r and ψ_r angles. Similar to the CPS, the DCPS also provides a signature of the target (91×181). To generate a DCPS, two sets of information from the $\mathbf{C_2}$ matrix are required, either from two distinct targets or, as utilized in this study, from a specific point location or parcel acquired at two separate dates. In this study, we use the latter, i.e., the $\mathbf{C_2}$ matrix of a point location acquired at two different dates. The two $\mathbf{C_2}$ are first used individually to generate two CPSs. Subsequently, these two CPSs are used to generate the DCPS

$$\text{DCPS} = \log_{10}\left(\frac{P_{\text{CP}(t=n)}}{P_{\text{CP}(t=0)}}\right) \tag{5}$$

where $P_{\text{CP}(t=0)}$ is the synthesized received power (of size 91×181) at a reference data (example, the first acquisition data) and $P_{\text{CP}(t=n)}$ is the synthesized received power (of size 91×181) at the nth acquisition (example, at second, third, and n acquisition date).

This work employs five RCM images acquired between July and September 2021. The temporal datasets capture the crop growth during the summer season. The images were coregistered to ensure consistent analysis, and a common subset was considered to cover the same geographical region. For the multi-date study of DCPS, one can consider the sequence of ascending and descending images separately to ensure that factors such as incidence angle will not affect the analysis. For instance, in this study, we selected the RCM image of the first acquisition date in ascending mode (i.e., 1 July 2021) as the master image, and the remaining two ascending acquisitions, captured on 30 July and 27 August 2021, as slave images. The DCPS was then generated based on the CPS of each slave image with the reference image to assess change in the crop fields over time.

C. Geodesic Distance (GD) Between CPSs

In this work, we introduce another essential parameter developed to facilitate the discrimination of targets by leveraging the entire space of CPS, represented as a matrix of dimensions 91×181. The computation of the GD between CPSs, denoted as GD_{CPS} is based on the formulation proposed in the work by Ratha et al. [40]. The two signatures can either be computed from the $\mathbf{C_2}$ matrices of two distinct targets or from the same point location (or a particular parcel) acquired on two dates. The GD_{CPS} serves as an effective metric for assessing the dissimilarity between two CPSs. A high value of GD_{CPS} infers that the two CPSs are different, whereas a low value of GD_{CPS} implies similarity.

In the context of temporal analysis, a high value of GD_{CPS} indicates the dynamic scattering nature of the target. However, a low value of GD_{CPS} infers no significant change. For example, built-up areas, permanent water bodies, etc., will result in low GD_{CPS} values, whereas croplands, forest areas, wetlands, etc., will result in high values of GD_{CPS}. Thus, using two CPSs for a target at two separate acquisition dates, we calculate the GD_{CPS} as

$$\text{GD}_{\text{CPS}} = \frac{2}{\pi} \cos^{-1} \frac{\text{Tr}(A^T B)}{\sqrt{\text{Tr}(A^T A)}\sqrt{\text{Tr}(B^T B)}} \tag{6}$$

where A and B are the CPS (of size 91×181) for the first date (i.e., $P_{\text{CP}(t=0)}$) and the nth acquisition date (i.e., $P_{\text{CP}(t=n)}$), respectively. Tr is the trace operator and the superscript T denotes transpose.

Similar to DCPS, one needs a pair of images to compute GD_{CPS}. We selected the RCM image acquired on 1 July 2021 as the master (reference) image. We used the other two ascending RCM images acquired on 30 July and 27 August 2021 as slave

images to compute the GD_{CPS} between the two corresponding dates. Therefore, for k acquired images, one will have $(k-1)$ images of GD_{CPS}. The GD_{CPS} parameter quantifies the temporal change of a target utilizing the entire CPS space.

D. Scattering Power Components

Numerous prior studies have introduced approaches to decompose the total scattered power into distinct components: Even-bounce, odd-bounce, and random (or diffused) scattering power components [36], [41], [42], [43], [44]. These approaches help comprehend the prevalent scattering mechanisms exhibited by a target, thereby, facilitating a more insightful characterization.

In this work, we formulate a parameter, designate it as μ using the CPS concept, and propose an alternative approach to decompose the total power g_0. We denote this alternate approach as $\mu - \chi$. We define the parameter μ as the ratio of the total polarized power to the maximum received power

$$\mu = 1 - \frac{P_{\min}}{P_{\max}} = \frac{P_{\max} - P_{\min}}{P_{\max}} \tag{7}$$

where $P_{\max}$ and $P_{\min}$ represent the maximum and minimum received powers, respectively. The ratio $P_{\min}/P_{\max}$ bears similarity to the pedestal height obtained from FP co-pol signature [45]. The quantity $P_{\max} - P_{\min}$ corresponds to the total polarized power in the CP-SAR mode.

Note that although similar, the parameter μ is not the same as the degree of polarization (m), which is the ratio of the polarized power to the total scattered power (g_0). In contrast, the parameter μ is the ratio of the polarized power to the maximum received power $P_{\max}$. These two quantities are equal when the scattered wave is either completely polarized or completely unpolarized. However, for partially polarized waves, the two quantities are unequal: $\mu \geq m$. The parameter μ derived from CPS quantifies the polarization structure with respect to the dominant scattering phenomena.

Utilizing the parameter μ, we decompose g_0 into two components: the matched power μg_0 and the unmatched power $(1-\mu)g_0$. The maximum power $P_{\max}$ is received when the polarization state of the scattered wave aligns with the receiving antenna's polarization state. Conversely, the minimum power $P_{\min}$ is received when the polarization state of the scattered wave is entirely unmatched (orthogonal) to the receiving antenna's polarization state. It is important to note that we can obtain $P_{\max}$ and $P_{\min}$ by synthesizing all polarization bases using CPS in this study.

We decompose the total power g_0 using μ and parameters derived from the Stokes vector $\boldsymbol{g_s}$ as

$$P_v = g_0\,(1-\mu) \tag{8}$$

$$P_s = \frac{1}{2}\mu\, g_0\,(1 - \mathrm{DoC}) \tag{9}$$

$$P_d = \frac{1}{2}\mu\, g_0\,(1 + \mathrm{DoC}) \tag{10}$$

where, P_v denotes the unmatched power, P_s corresponds to the odd-bounce matched power, and P_d represents the even-bounce matched power. The degree of circularity $\mathrm{DoC} = \pm \sin 2\chi$ depends upon the handedness of the transmitted circularly polarized wave. The $\pm$ sign signifies L circular and R circular transmit polarization, respectively. The ellipticity angle of the scattered wave is denoted by χ.

In contrast to previous works [41], [44], which decompose the total power g_0 into polarized and unpolarized components with the help of degree of polarization m, our approach involves the separation of g_0 into matched and unmatched power components using μ. One can express the difference between the two quantities as

$$\Delta = g_0(\mu - m) \geq 0 \tag{11}$$

which is the excess power over polarized power.

In a fully polarized wave scenario, where $\mu = m = 1$, the parameter $\Delta = 0$. Conversely, for a completely unpolarized wave with μ and m equal to zero, $\Delta = 0$ signifies no discrepancy in power computed using the two methods. However, the powers obtained using the two methods will differ for a partially polarized wave, where $\mu > m$.

TABLE I
OPTIMAL VALUES OF TUNING PARAMETERS FOR THE RF CLASSIFIER

#	Hyperparameter	Value
1	Number of decision trees	100
2	Number of variables in each node split	$\sqrt{\text{number of variables}}$
3	Minimum size of a terminal node	2
4	Fraction of the input to bag per tree	0.5
5	Number of random seeds	5

E. Classification Scenarios

RF is a powerful machine learning classification technique known for its robustness and accuracy in handling complex datasets. By creating an ensemble of decision trees trained on random subsets of data and features, RF aggregates results for final predictions [46]. Noteworthy is its ability to handle high-dimensional datasets, automatically selecting informative features, reducing overfitting, and accommodating missing values and outliers [30], [47]. Particularly suited for remote sensing mapping tasks, RF handles diverse data types, provides variable importance estimates, and captures nonlinear relationships [48], making it a valuable tool for generating reliable and interpretable results in complex spatial patterns.

Various tuning parameters are used in RF implementation: fraction of the input to bag per tree, the number of decision trees to create per class, the number of variables per split, and the minimum size of a terminal node [49]. This study utilizes a grid search optimization process to determine the optimal values for RF hyperparameters. The chosen parameter values are detailed in Table I, providing a comprehensive overview of the specific RF configuration employed in our research.

Table II lists the features used in the classification task. Numerous studies have demonstrated the ability of polarimetric parameters derived from CP-SAR data for improved crop classification using the RF classification technique [26], [29].

TABLE II
LIST OF FEATURES EXTRACTED FROM THE RCM CP DATA AND INCLUDED IN THE CLASSIFICATION RUNS

Feature Type	Description	Symbol	Reference
Intensity Channels	backscatter coefficients	σ^0_{RH}, σ^0_{RV}	-
Wave Descriptors	conformity coefficient	μ_0	[31]
	relative phase	δ	[31]
	circular polarization ratio	μ_c	[31]
CP Decompositions	$m-\chi$ odd-bounce component	$m\chi_0$	[41]
	$m-\chi$ double-bounce component	$m\chi_e$	[41]
	$m-\chi$ volume/random scattering component	$m\chi_v$	[41]
	$\mu-\chi$ odd-bounce component	P_s	[54]
	$\mu-\chi$ double-bounce component	P_v	[54]
	$\mu-\chi$ volume/random scattering component	P_d	[54]
CP Signature	GD between two CPSs	$\mathrm{GD}_{\mathrm{CPS}}$	Proposed

TABLE III
DEFINED SCENARIOS FOR CROP MAPPING BY CP-SAR DATA IN THIS STUDY

#Scenario	Description	Input Feature Combination	Scenario Objective
S1	$\mu-\chi$ versus $m-\chi$ components	(σ^0_{RH}, σ^0_{RV}), (P_d,P_v,P_s), ($m\chi_{\mathrm{o}}$,$m\chi_{\mathrm{e}}$,$m\chi_{\mathrm{v}}$)	A comparative analysis of $m-\chi$ and $\mu-\chi$
S2	Single-date versus multi-date crop mapping	(σ^0_{RH}, σ^0_{RV}), (P_d,P_v,P_s), ($m\chi_{\mathrm{o}}$,$m\chi_{\mathrm{e}}$,$m\chi_{\mathrm{v}}$), ($\mathrm{GD}_{\mathrm{CPS}}$, μ, δ, μ_c)	A comparative analysis of single-date and multi-date features

Among them, scattering power components derived from decomposition techniques, such as the $m-\chi$ decomposition [41] have been reported to yield better classification results [29], [50], [51]. The temporal variation in these power components as the crop advances helps the RF classifier with enhanced distinction between the crop types. This study utilizes the scattering power components obtained from the $\mu-\chi$ decomposition technique to classify various crops using the RF classifier.

Further, the conformity coefficient is a valuable metric in discerning different scattering mechanisms from crops and has proven beneficial in their mapping [26], [52]. In addition, studies have also examined polarimetric parameters derived from simulated CP-SAR data, such as the degree of polarization, relative phase, and the circular polarization ratio for crop monitoring and biophysical parameter estimation [35], [53]. The RF classifier adeptly manages the diverse ranges of these polarimetric parameters and, furthermore, provides feature importance estimates. We discuss the feature importance of the various polarimetric descriptors used in this study for crop classification in Section IV-D3.

Table III summarizes the defined scenarios and the selected feature combinations for crop mapping using CP-SAR data. In this work, two image classification scenarios were designed to evaluate and learn the influence of feature combinations on the classification accuracy of four crop classes based on RF. The classification results between the features extracted from $\mu-\chi$ and $m-\chi$ are compared in the first scenario. In the second scenario, a comparative analysis of classification accuracy is conducted, evaluating both single-date and multi-date feature combinations. These combinations were used in this study to compare and assess the capabilities of each type of data and their combinations in classifying crop types. Moreover, integrating the additional features in the second scenario was meant to evaluate the effectiveness of data integration in SAR-based crop mapping. Our study applied the same training and testing samples to different feature combinations in RF classification, allowing for direct accuracy comparison between different scenarios using varying input features.

III. STUDY AREA AND DATASET

A. Study Area

The experiment was conducted in a sprawling agricultural region situated in southern Quebec, Canada. Encompassing a substantial geographical expanse ranging from W72°46′50″ to W73°8′0″ longitude and N45°55′30″ to N46°4′0″ latitude, the study area spans approximately 450 km^2 . The area is visually represented in Fig. 2. This agricultural terrain is characterized by natural boundaries, with Lac Saint-Pierre Lake enveloping the northern periphery, the Richelieu River delineating the western edge, and the Saint-François River marking the eastern boundary. The Yamaska River meanders through the study area from south to north, ultimately converging with the Saint-Lawrence River at Lac Saint-Pierre Lake. This diverse agricultural landscape hosts various crops, including soybean, hay, oats, wheat, barley, and corn, among others.

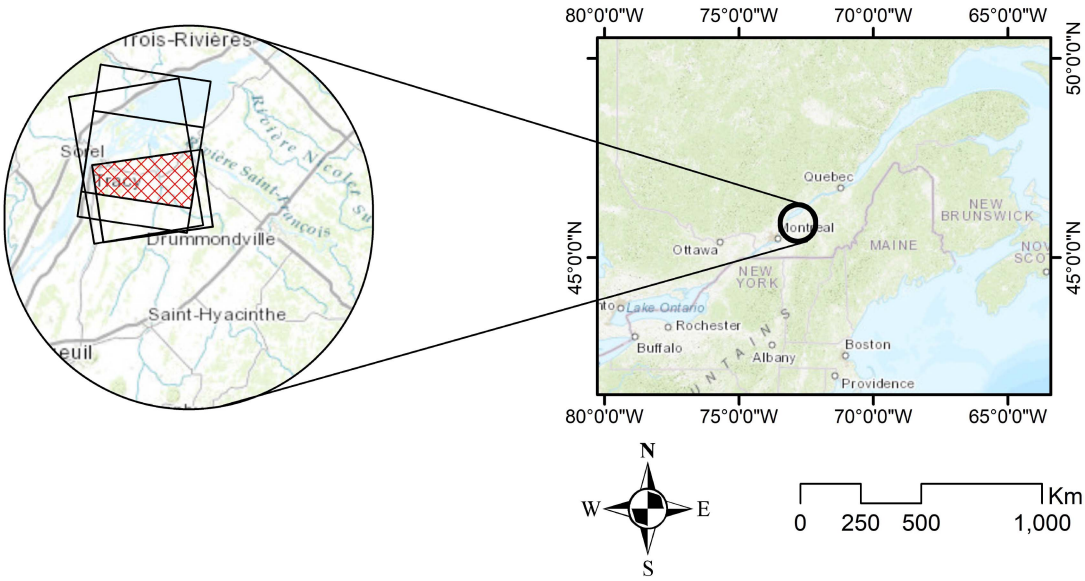

Fig. 2. Location of the study area with coverage and overlay of ascending and descending RCM acquisitions.

TABLE IV
THIS STUDY USES BOTH ASCENDING AND DESCENDING RCM IMAGES

#	Satellite	Acquisition Date	Incidence Angle	Orbit Pass	Beam Mode	Resolution (rg×az)	Polarization	Looking Direction	Swath width
1	RCM1	2021-07-01	40.01°–42.01°	Ascending	High Resolution (StripMap)	2.8 m×2.5 m	(RH, RV)	Right Looking	30 km
2	RCM2	2021-07-30	49.31°–50.87°						
3	RCM3	2021-08-27	49.31°–50.87°						
4	RCM1	2021-07-30	45.61°–47.34°	Descending					
5	RCM2	2021-08-15	45.61°–47.34°						

B. RCM Time-Series Data and Preprocessing

In this work, we processed a set of five single look complex RCM frames acquired between 1 July and 27 August 2021, spanning the duration of the crop growth. The images were captured with a nominal spatial resolution of 5 m and with the supported stripmap beam mode. The coverage areas of the employed RCM images over the study area are depicted in Fig. 2, and their details are tabulated in Table IV. For effective land cover classification and other EO applications, preprocessing of SAR data plays a critical role. In this study, we preprocessed the RCM images in the SNAP software following the standard processing steps outlined in [29]. The initial steps involve calibration, where we transform the digital channels (RH, RV) data of the RCM images into the sigma-naught backscattering coefficient (σ^0) measured in decibel. To reduce speckle noise and generate a ground range square pixel, we multilook the images with two looks in azimuth and range (2×2).

Subsequently, we derived the 2×2 covariance ($\mathbf{C}_2$) matrix from each pixel of the SAR image using the "polarimetric matrix generation" toolbox, facilitating the application of polarimetric decomposition to determine various scattering mechanisms. The inherent variability in radar look angles during SAR data acquisition, coupled with the influence of topography, often leads to distortions in the resulting images. To mitigate these distortions, we performed terrain correction on the 2×2 $\mathbf{C}_2$ matrix. This correction was executed using SNAP's `Range Doppler Terrain Correction` module, incorporating the SRTM 1 arcsec digital elevation model. The primary objective of this terrain correction process is to rectify the geometric distortions present in SAR imagery. By aligning the geometric representation of the images with the actual topography, we aim to enhance the accuracy and reliability of the spatial information captured in the imagery. This correction is crucial for ensuring that SAR data better aligns with the real-world terrain features [46], [55].

Moreover, we implemented an average (boxcar) filtering procedure using a 3×3 pixel window to mitigate the influence of speckle noise. Following the noise reduction step, the data was subset to focus exclusively on the test site. We, then, performed the coregistration process of the multitemporal images to properly align them with a root-mean-square error of 1.12 m. The coregistration was performed using the first date RCM data, acquired on 1 July 2021, as the master image while treating the subsequent dates as slave images.

TABLE V
DETAILS OF CROPLAND COVER TYPES DELINEATED IN THE GROUND-TRUTH DATA WITH THE NUMBER OF TRAINING AND TESTING POLYGONS FOR EACH CROP PRODUCTION GROUP

Description			#Total Samples	#Training Samples	#Testing Samples
Label	Production Group	Production type/class			
Soybean	Soybean	Soybean IP (Identity Preserved), Seed Soybeans, Soybean	1158	232	926
Hay	Hay	Hay Option Need Food, Hay, Hay Area Option, Pasture, Forage Soybeans	275	57	218
Cereal	Oats	Oats	221	46	175
	Wheat, Triticale, Spelled	Human Food Autumn Wheat, Animal Spring Wheat, Human Spring Wheat, Food Seed Wheat			
	Barley	Barley, Seed Barley			
Corn	Forage Corn	Fodder Corn Area Option, Forage Corn	1371	275	1096
	Grain Corn	Grain Corn			
Total			3025	610	2415

The training and testing samples were splitted with a ratio of 20-80%.
*Note: The same color codes are used in classification maps.

C. Reference Data

The availability of ground-truth land cover labels is pivotal for training and validating supervised classifiers in remote sensing. The absence of such reference data can lead to suboptimal classification performance and challenges in result evaluation [4], [56]. While ground-truth data is invaluable for supervised classification tasks, obtaining it presents significant challenges, particularly for expansive areas. Ground-truth labels should be collected through field surveys/visits to collect first-hand and high-fidelity information [57], [58]. However, these endeavors are constrained by the substantial investment of time and human labor they demand. To address this challenge, one pragmatic approach is to leverage well-established official products, such as the BDPPAD (Base de données des parcelles et productions agricoles déclarées), as a surrogate for ground-truth data.

The BDPPAD database of declared agricultural parcels and productions contains a series of polygons provided in vector format to represent the outline of delineated agricultural parcels associated with the Agricultural Financial Corporation of Quebec (FADQ) client files. The purpose of this database is to provide the most reliable overview possible of the crops contained in a plot for a given season. This data is used as the reference or ground-truth information in this study, which covers a part of the agricultural territory of Quebec. Since the primary purpose of the current study is to characterize crops using the newly proposed features/descriptors rather than generating a crop inventory map, we made suitable adjustments in the reference database of the study area. Thus, we selectively omitted/grouped some classes in the following cases (rules for ground-truth codes production).

1) *Integration:* A pragmatic approach has been adopted since the agricultural production data from FADQ cannot be treated as an updated ground-truth. In this regard, similar crop yields have been grouped and aggregated into a single class. Consequently, each parcel or shapefile is assigned to only one crop type.
2) *Simplification:* Specific categories were excluded from consideration to optimize processing efficiency and focus on relevant classes for this study. Classes, such as vegetables not pertinent to the scope of this research and regions with multiple crops in close proximity, were omitted and designated as background.
3) *Exclusion:* Specific categories characterized by a limited number of reference samples and minimal spatial coverage were intentionally excluded from the database to mitigate the challenges associated with differentiation and potential misclassification.

In the comprehensive categorization of agricultural fields within the study area, class codes have been organized into a standardized set of four primary crop categories: 1) soybean, (2) hay, (3) cereal, and (4) corn. Refer to Table V and Fig. 3 for a visual representation of these crop categories. This study, therefore, aims to map and analyze the characteristics of these essential food sources. Notably, corn and soybean emerge as the predominant crop types, holding the largest share within the study site. These crops are distributed across the study region, with corn fields exhibiting characteristics of concentration in

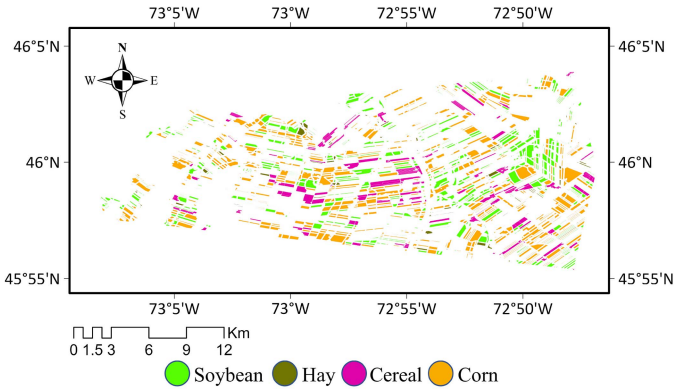

Fig. 3. Ground-truth data for agricultural fields.

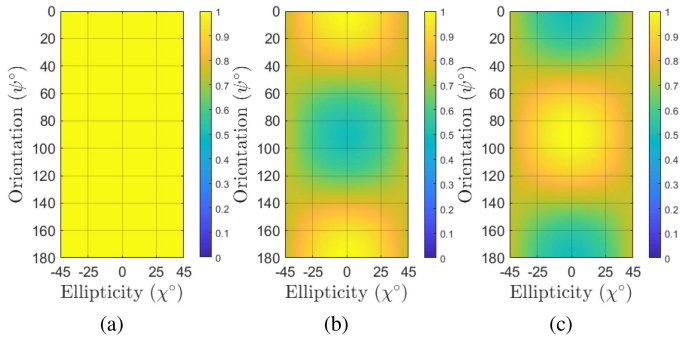

Fig. 4. CPS of different volume models constituted by (a) a mixture of randomly oriented dipoles (RD), (b) a mixture of horizontal dipoles (HD), and (c) a mixture of vertical dipoles (VD).

certain instances. It is important to highlight that a supervised classifier was employed as part of the methodology, with 20% of the polygons (delineations) utilized for selecting training samples, whereas the remaining 80% served as testing points for the classifier.

IV. Experimental Results and Analysis

This section presents a detailed analysis of the CPS for different crop types. Further, we utilize multitemporal RCM data sets acquired over these crop types to compute the DCPS and GD between two CPSs calculated from two images acquired at two different dates. Here, we calculate the DCPS and GD by considering the first acquired image, i.e., 1 July, as the reference image. We, then, use parameters derived from CPS to compute the three scattering power components. Furthermore, we classify crop types using descriptors obtained from CPS and $\mu - \chi$ decomposition for different scenarios (Table III).

A. Analysis of CPS for Different Crop-Types

Leveraging the ground-truth data, we systematically identified and sampled pixels corresponding to soybean, hay, corn, and cereal crops from the processed RCM images to generate the CPS. The temporal variations in the CPS for these crops are shown in Figs. 5–8, respectively. In the literature [59], [60], scattering from crop canopy is usually modeled by a cloud of randomly oriented, very thin, dipole-like scatterers. It provides crucial insights into understanding the scattering mechanism from the crops at their various growth stages. Thus, for enhanced understanding of the scattering from the crops, we display the CPS of volume models constituted by the following:

1) a mixture of randomly oriented dipoles (RD);
2) a mixture of horizontal dipoles (HD);
3) a mixture of vertical dipoles (VD) in Fig. 4.

In Fig. 5(a), one can note that the CPS for soybean on 1 July exhibits a characteristic similarity to a trihedral target. It is because for a R circular transmit ($\chi = -45^\circ$) the sense of the scattered wave from trihedral changes (orthogonally polarized), and hence, the maximum power is received at around $\chi = 45^\circ$. Specifically, the maximum power ($P_{\max}$) is received for $\chi = 22^\circ$ and $\psi = 24^\circ$ (Table VI). The distinctive CPS pattern indicates prevalent surface scattering from soybean on 1 July. This observation suggests that the incident wave interacts more significantly with the underlying surface during the early crop stage than with the plant components. In addition, the high values of $\mu = 0.85$ further support the inference of pure scattering from soybean during this period.

With progress in the crop stage, the CPS starts to change, as seen from Fig. 5(b). On 30 July, μ decreased to 0.68 as the scattering purity reduced due to the interaction of the incident waves with the grown crop components. We observed high values of received power for $\chi = 0^\circ$ (i.e., for linear waves) during this time (Table VI).

Further, as the soybean crop progressed, we found the μ to reduce to 0.59. The low values of purity caused by uncertainty in the determination of the polarization structure of the scattered wave indicate random (or diffused) scattering from the crop on 27 August. On comparing the observed CPS of soyabean with volume models constituted of different mixtures of dipoles (Fig. 4), we found it similar to the CPS of a mixture of vertical dipoles. The maximum power was received for $\chi = -6^\circ$ and $\psi = 71^\circ$ (nearly linear vertical), indicating that the incident waves interacted extensively with the vertically aligned crop components during this time (Table VI).

The CPSs discussed above are generated using the ascending orbit RCM images. However, for 30 July and 15 August, RCM descending orbit images were also acquired over the test site. Notably, a distinctive observation emerges for 30 July, where the CPS generated from the ascending [Fig. 5(b)] and descending [Fig. 5(d)] orbit RCM images exhibit marked differences. On 30 July, the CPS derived from the descending RCM image showcases characteristic similarity to a vertical dipole. The maximum received power during this time was observed for $\chi = 10^\circ$ and $\psi = 92^\circ$, as detailed in Table VI. It is possible because, for the descending orbit, the orientation of the soybean fields for the radar line of sight might have changed, resulting in scattering similar to a vertical dipole.

The CPS for the hay crop, as shown in Fig. 6, exhibits temporal variations that offer insights into the scattering characteristics during different stages of crop growth. On 1 July, the CPS suggests scattering from a random target, with low values of

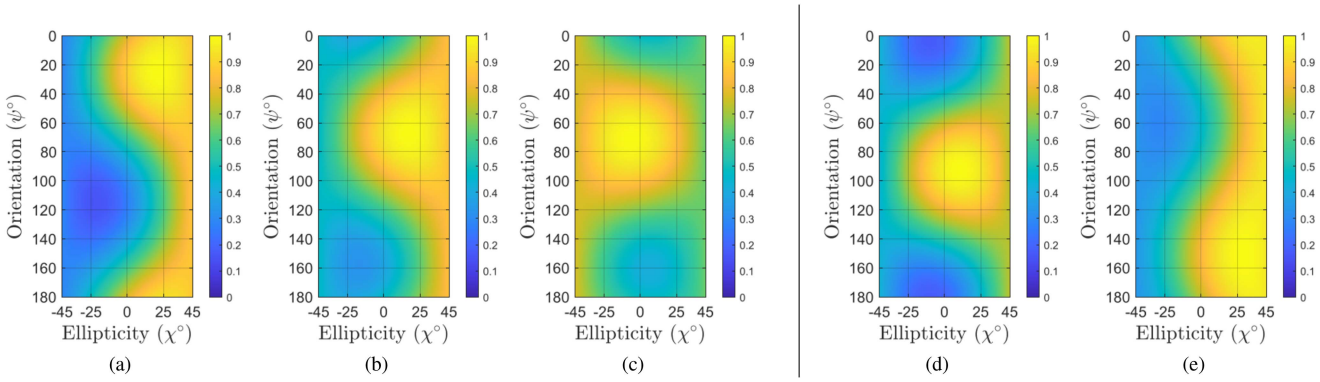

Fig. 5. Temporal variation of CPS for the soybean: (a) 1 July, (b) 30 July, (c) 27 August, (d) 30 July, and (e) 15 August. The vertical line separates the CPS of the ascending and descending images.

TABLE VI
CPS RESPONSES OF SOYBEAN, HAY, CORN, AND CEREAL FOR SOME SPECIFIC ELLIPTICITY (χ) ANGLES AND ORIENTATION (ψ) ANGLES

		Soybean					**Hay**				
Parameters		**Ascending**			**Descending**		**Ascending**			**Descending**	
χ	ψ	1 Jul.	30 Jul.	27 Aug.	30 Jul.	15 Aug.	1 Jul.	30 Jul.	27 Aug.	30 Jul.	15 Aug.
0°	0°	0.78	0.47	0.48	0.2	0.74	0.84	0.25	0.53	0.94	0.41
0°	90°	0.37	0.86	0.93	0.97	0.55	0.70	1	0.73	0.45	0.71
0°	45°	0.81	0.86	0.88	0.55	0.5	0.62	0.63	0.51	0.64	0.57
45°	0°	0.87	0.85	0.64	0.73	0.95	0.93	0.67	0.97	0.63	0.97
-45°	0°	0.29	0.47	0.77	0.44	0.34	0.61	0.57	0.3	0.52	0.16
μ		0.85	0.68	0.59	0.83	0.71	0.46	0.76	0.74	0.87	0.87
$\chi_{\max}$		22°	17°	-6°	10°	29°	22°	0°	32°	-16°	35°
$\psi_{\max}$		24°	67°	71°	92°	151°	148°	90°	115°	172°	90°
		Corn					**Cereal**				
Parameters		**Ascending**			**Descending**		**Ascending**			**Descending**	
χ	ψ	1 Jul.	30 Jul.	27 Aug.	30 Jul.	15 Aug.	1 Jul.	30 Jul.	27 Aug.	30 Jul.	15 Aug.
0°	0°	1	0.7	0.83	0.97	0.61	0.96	0.43	0.51	0.71	0.54
0°	90°	0.3	0.74	0.47	0.37	0.63	0.59	0.69	0.87	0.96	0.98
0°	45°	0.68	0.78	0.62	0.62	0.81	0.74	0.57	0.83	0.8	0.7
45°	0°	0.67	0.99	0.95	0.8	0.95	0.9	0.98	0.90	0.93	0.84
-45°	0°	0.62	0.45	0.35	0.53	0.29	0.66	0.14	0.49	0.74	0.68
μ		0.71	0.56	0.7	0.66	0.76	0.45	0.89	0.62	0.32	0.48
$\chi_{\max}$		0°	38°	29°	12°	30°	16°	36°	21°	18°	10°
$\psi_{\max}$		0°	55°	176°	176°	46°	174°	86°	71°	100°	97°

$\mu = 0.46$, indicative of random or diffused scattering from the crop at that time.

As the hay crop progresses, on 30 July, the CPS takes on characteristics similar to a vertical dipole [Fig. 6(b)]. The maximum received power is observed for $\chi = 0^\circ$ and $\psi = 90^\circ$ (linear vertical), signifying the interaction of incident waves with the vertically aligned hay crops (Table VI). Subsequently, in Fig. 6(c), high received power (0.97) is observed for $\chi = 45^\circ$ (Table VI), likely attributed to surface scattering from the underlying soil layer as the hay crop undergoes drying, affecting its dielectric properties. Further, the increase in μ to 0.74 on 27 August indicates a transition to pure scattering from the hay crop, emphasizing the evolving nature of the scattering behavior with crop development.

The CPS of the hay crop, derived from the descending orbit RCM images, are presented in Fig. 6(d) and (e). These descending orbit CPS offer complementary information about the crop and its growth stages, enhancing our understanding of the scattering characteristics. The observed variation in CPS between ascending and descending orbits can be attributed to changes in crop (field) orientation concerning the radar line of sight and overall geometric differences.

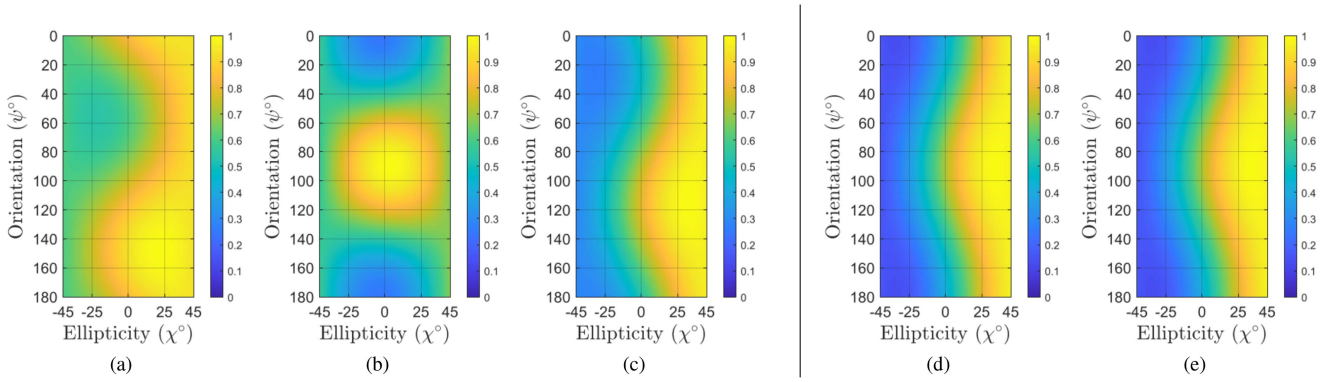

Fig. 6. Temporal variation of CPS for the hay crop: (a) 1 July, (b) 30 July, (c) 27 August, (d) 30 July, and (e) 15 August. The vertical line separates the CPS of the ascending and descending images.

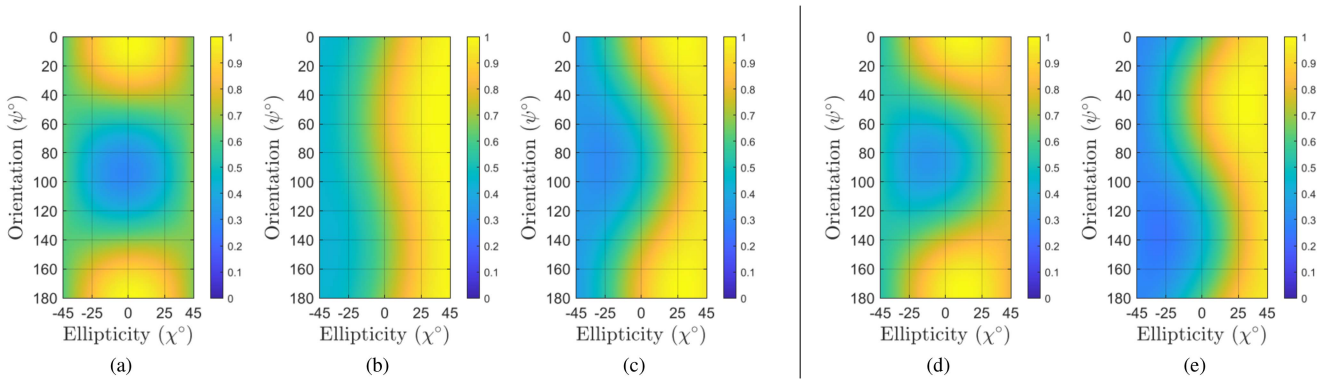

Fig. 7. Temporal variation of CPS for the corn crop: (a) 1 July, (b) 30 July, (c) 27 August, (d) 30 July, and (e) 15 August. The vertical line separates the CPS of the ascending and descending images.

Notably, the CPS exhibits similarities to a trihedral target for the descending orbit between 30 July and 15 August. This resemblance may arise from the incident waves primarily interacting with the top canopy layer of the crop for the descending orbit, resulting in surface scattering. Supporting this interpretation are the high values of $\mu = 0.87$ observed for the hay crop during this period, indicating a predominant surface scattering contribution.

In Fig. 7, the temporal evolution of the CPS for corn, showing changes in the crop stage, is presented. Fig. 7(a) indicates that the CPS of the corn crop on 1 July resembles that of a horizontal dipole. This could be attributed to the incident waves interacting more prominently with the underlying ground and the crop's small stems during the initial growth stages. This interaction results in a combination of odd-bounce and even-bounce scattering, with maximum power received for $\chi = 0^\circ$ and $\psi = 0^\circ$ indicating strong returns when waves are horizontal (refer to Table VI).

As the crop progresses, the CPS transforms, as shown in Fig. 7(b) and (c), resembling similar to a trihedral target on 30 July and 27 August. This shift is attributed to the limited penetration capability of incident C-band waves; thus, mainly interacting with the broad corn leaves and resulting in surface scattering. This interpretation aligns with the observed high values of received power for $\chi = 45^\circ$ (see Table VI).

The CPS of corn, generated from descending orbit RCM images, exhibits noteworthy characteristics. On 30 July [Fig. 7(d)], the CPS appears similar to a horizontal dipole, with the maximum power received for $\chi = 12^\circ$ and $\psi = 176^\circ$. This suggests an extended interaction of the incident wave with the horizontal crop components (refer to Table VI). Similarly, on 15 August [Fig. 7(e)], the CPS takes on the form of a trihedral, with the maximum power received for $\chi = 30^\circ$. This indicates the dominant surface scattering from the crop during this period.

The CPS of cereal crops, as illustrated in Fig. 8, exhibits notable variations. On 1 July, when the cereal crops were heading toward the flowering growth stage, Fig. 8(a) suggests random scattering depicted in the CPS, resembling a mixture of horizontal dipoles [as shown in Fig. 4(b)]. This is supported by a low value of $\mu = 0.45$, with the maximum power received at $\chi = 16^\circ$ and $\psi = 174^\circ$ indicating scattering close to a horizontal dipole (see Table VI).

As the crop advances to the fruit development stage, the C-band incident wave interaction is limited to the top canopy layers; the CPS on 30 July takes on characteristics similar to a trihedral target [Fig. 8(b)]. The observed $\mu = 0.89$ indicates pure

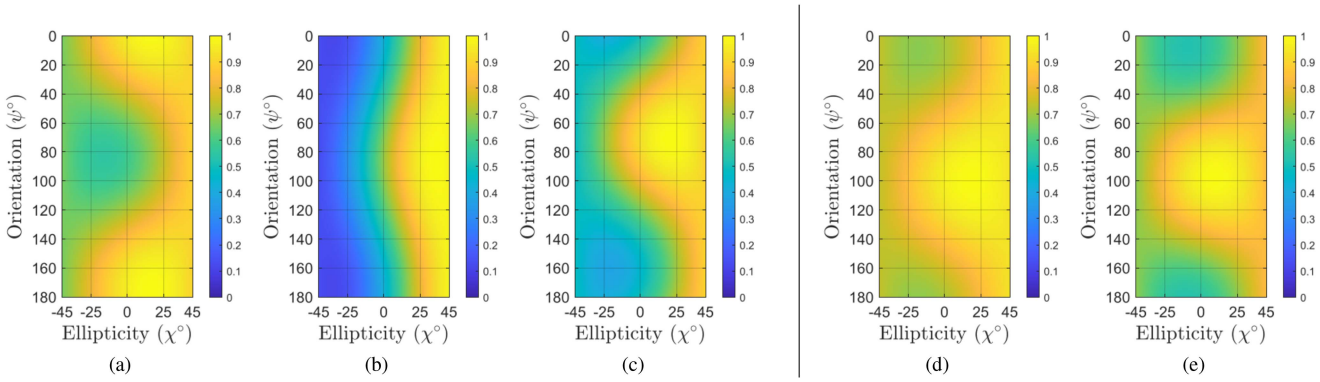

Fig. 8. Temporal variation of CPS for the cereal crops: (a) 1 July, (b) 30 July, (c) 27 August, (d) 30 July, and (e) 15 August. The vertical line separates the CPS of the ascending and descending images.

scattering from the cereal crop during this time. The maximum power is received for $\chi = 36^\circ$, indicating surface scattering from the cereal crop on 30 July.

On 27 August, as the cereal crops reach their senescence stage, the CPS infers a mixture of scattering resembling both a trihedral and a vertical dipole target [Fig. 8(c)]. This could be attributed to the extended interaction of the incident wave with cereal crops during this stage. The maximum power is received at $\chi = 21^\circ$ and $\psi = 71^\circ$, with a corresponding μ value of 0.62 (refer to Table VI).

However, the CPS generated from the descending RCM image indicates predominant random (or diffused) scattering from the cereal crop on 30 July [Fig. 8(d)]. This observation aligns closely with the CPS of a random mixture of dipoles [as depicted in Fig. 4(a)]. In addition, the low value of $\mu = 0.32$ during this time, as detailed in Table VI, further supports this interpretation. This discrepancy in scattering behavior between ascending and descending orbits suggests that changes in crop orientation (fields) due to changes in satellite orbit passes can influence the interaction of incident waves with the crop canopy. This change results in diffused scattering and a predominance of random scattering characteristics.

B. Analysis of DCPS and GD for Different Crop-Types

This section quantifies variations between the CPS generated for two observation dates using the DCPS descriptor. The DCPS provides information as a signature plot similar to the CPS represented as a matrix of dimensions 91×181, exemplified in Fig. 9. The goal is to assess the differences between two CPSs through the GD metric, yielding a scalar quantity between 0 and 1. For DCPS, when two CPSs exhibit similar scattering mechanisms, the values will be close to 0 across all combinations of χ and ψ. However, maximum values will be observed at χ and ψ with an orthogonal scattering mechanism between the two CPSs. Similarly, GD will have a value of 0 for two similar scattering scenarios, whereas two CPSs indicating orthogonal scattering mechanisms will yield a value of 1.

It is important to note that the analysis utilizes three ascending orbit RCM images for DCPS and GD assessments. Fig. 9(a) and (b) illustrate the DCPS of soybean between CPSs of 1 July – 30 July and 1 July – 27 August, respectively. The maximum variation between the CPSs on 1 July and 30 July is observed around $\chi = -20^\circ$ and $\psi = 110^\circ$. This is attributed to the change in scattering from soybean during the acquisition dates, transitioning from trihedral to vertical dipole scattering. Similarly, between 1 July and 27 August, the DCPS exhibits maximum values around $\chi = -18^\circ$ and $\psi = 110^\circ$.

Similarly, in the case of the hay crop, the maximum variation between the CPS on 1 July and 30 July was observed around $\chi = 10^\circ$ and $\psi = 82^\circ$. The DCPS analysis reveals a transition from trihedral to vertical dipole scattering during this period [Fig. 9(c)]. Examining the DCPS of the hay crop between 1 July and 27 August indicates a shift from random to surface scattering [Fig. 9(d)].

For corn, the DCPS analysis indicates a significant alteration in scattering between 1 July and 30 July, primarily around $\chi = 7^\circ$ and $\psi = 87^\circ$ [Fig. 9(e)]. Similarly, from 1 July to 27 August, the most substantial change in scattering was observed around $\chi = 18^\circ$ and $\psi = 103^\circ$. This shift is attributed to the advanced crop stage, where the CPS exhibited similarity to a trihedral due to the limited penetration of incident C-band waves.

Similarly, the DCPS analysis of cereal crops between 1 July and 30 July reveals a shift in scattering from random to surface phenomena [Fig. 9(g)]. This transformation is attributed to the prevalence of random scattering on 1 July during the heading to the flowering stage, whereas surface scattering became dominant with further crop advancement. Likewise, the DCPS of cereal crops between 1 July and 27 August indicates a change in scattering from random to vertical dipole [Fig. 9(h)].

Moreover, the varied ranges of GD values for each crop type across the two time intervals offer crucial insights into the subtle temporal changes in their CPS. GD values present a quantitative and sensitive approach to discern the temporal alterations in crop scattering behaviors, especially in the context of crop discrimination and monitoring. An illustrative example of GD computation between the RCM images acquired on 1 July and 30 July is presented in Fig. 10.

Fig. 11 presents box plots of the GD values for various crop types between two sets of RCM images. It is evident that hay

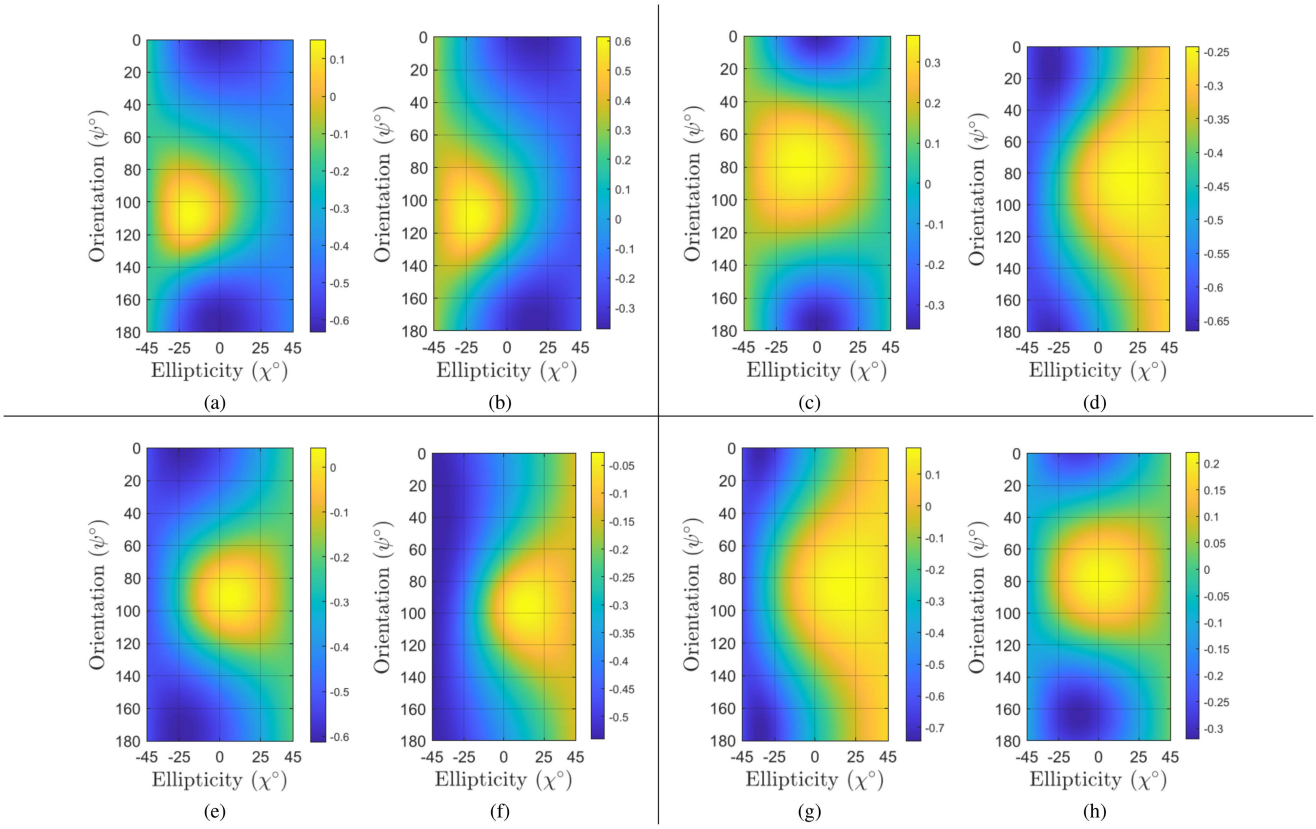

Fig. 9. Dynamic change analysis of crop types over time using DCPS concept and based on ascending RCM images considering the image acquired on 1 July (time 1) as the reference and the other two images acquired on 30 July (time 2) and 27 August (time 3) as slave. (a) and (b) soybean, (c) and (d) hay, (e) and (f) corn, and (g) and (h) cereal.

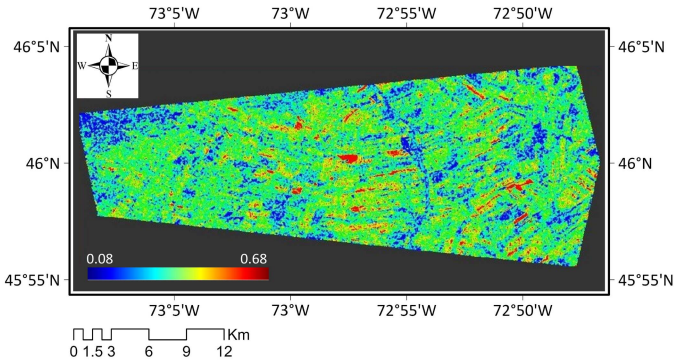

Fig. 10. Illustration of the GD between CPS of two ascending RCM images acquired on 1 July and 30 July.

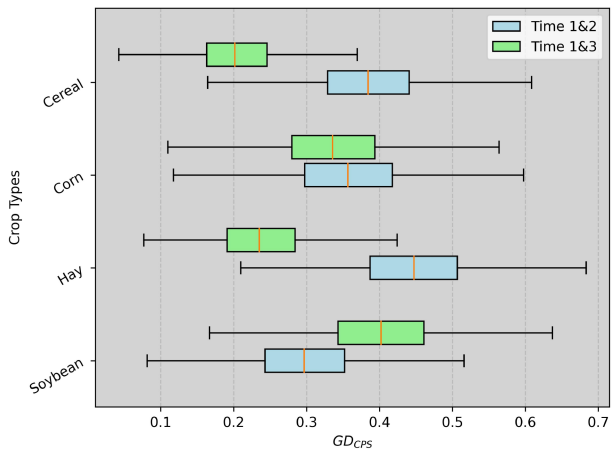

Fig. 11. Comparing the GD_{CPS} values for the crop types, considering the ascending RCM image acquired on 1 July (time 1) as the reference and the other two ascending images acquired on 30 July (time 2) and 27 August (time 3) as slave.

fields demonstrate comparatively higher GD values between RCM images acquired on 1 July and 30 July, indicating significant changes in scattering characteristics. This observation aligns with the nature of hay crops, which may undergo rapid growth in plant structure and alterations in moisture content. Conversely, crops like cereal exhibit lower GD values, suggesting relatively stable scattering behaviors over time.

These differences underscore the efficacy of GD values in discriminating between various crop types by capturing their distinct temporal behavior patterns. By utilizing the entire received power space (91×181), GD considers subtle variations in the temporal scattering behavior of crops, making it beneficial for their accurate classification.

C. Analysis of Scattering Power Components for Different Crop-Types

In this section, we explore the temporal variations in the three scattering power components of various crop types, which

TABLE VII
TEMPORAL VARIATION OF POWER COMPONENTS BASED ON $\mu - \chi$ DECOMPOSITION METHOD

	Soybean					Hay				
Component	**Ascending**			**Descending**		**Ascending**			**Descending**	
%	1 Jul.	30 Jul.	27 Aug.	30 Jul.	15 Aug.	1 Jul.	30 Jul.	27 Aug.	30 Jul.	15 Aug.
P_d	13.08	13.33	21.22	09.38	05.4	09.72	17.64	12.35	14.08	12.10
P_v	35.64	47.45	53.51	43.67	31.53	59.50	38.47	41.67	40.19	42.39
P_s	51.28	39.22	25.27	46.94	63.06	30.78	43.89	45.98	45.73	45.51
	Corn					**Cereal**				
Component	**Ascending**			**Descending**		**Ascending**			**Descending**	
%	1 Jul.	30 Jul.	27 Aug.	30 Jul.	15 Aug.	1 Jul.	30 Jul.	27 Aug.	30 Jul.	15 Aug.
P_d	34.53	19.10	12.32	16.85	09.57	30.14	21.28	11.05	22.24	08.33
P_v	40.56	49.19	46.57	48.31	43.61	47.59	26.85	41.87	57.45	42.89
P_s	24.91	31.71	41.09	34.83	46.80	22.27	51.87	47.08	20.31	48.78

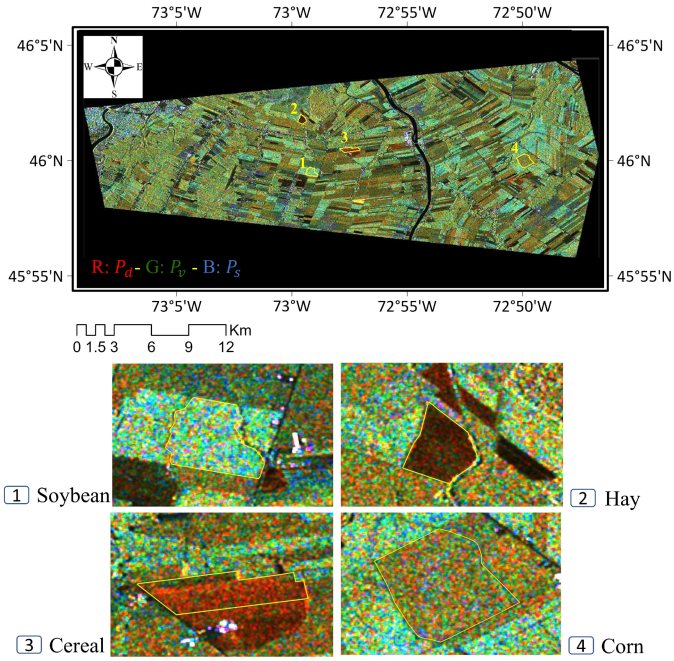

Fig. 12. RGB illustration of the three scattering power components of $\mu - \chi$ model during the peak of the growing season extracted from ascending RCM image acquired on 30 July, where red corresponds to P_d, green to P_v, and blue to P_s.

prove valuable in their classification. We employ the parameter μ derived from the CPS to extract the three scattering power components mentioned. These components, namely, P_d, P_s, and P_v represent the even-bounce matched power, odd-bounce matched power, and unmatched power, respectively.

In Fig. 12, we present the RGB composite of the three scattering power components derived from an ascending RCM image captured over the study area on 30 July. A zoomed-in area featuring four distinct crops is also depicted for enhanced interpretation. It is evident from Fig. 12 that the scattering powers exhibit substantial variations for different crops, reflecting the dominance of specific scattering characteristics associated with each crop.

We, then, quantitatively assess the temporal variations in the three scattering power components for different crops (Table VII). During the initial stage of soybean growth, we observed the dominance of P_s power (approximately 51%). This dominance could be attributed to the incident C-band waves penetrating the small soybean plants, interacting more with the underlying ground, and resulting in prevalent surface scattering.

The unmatched power P_v was at 35.64%, indicating marginal interaction of the incident waves with the small crop components (Table VII). As the crop progressed, we observed a significant increase in the P_v power to 47.45% on 30 July and 53.51% on 27 August.

Similarly, the P_s power exhibited a significant reduction during this period (Table VII). The notable increase in the P_v power component could be attributed to the interaction of the incident wave with the matured crop components, resulting in random (or diffused) scattering. Interestingly, the scattering powers derived from the descending pass RCM images showed a dominant P_s power on 30 July and 15 August. This observation may be attributed to changes in the orientation of the soybean crop (field) with respect to the radar line of sight, facilitating increased interaction of the incident wave with the underlying ground surface.

Further, for the hay crop, we observed a high P_v (59.50%) on 1 July, suggesting the dominance of random (or diffused) scattering (Table VII). However, on 30 July, we observed a dominance of P_s power (43.89%). During this time, the CPS was also close to a vertical dipole, indicating the interaction of the incident wave with the vertically aligned hay crops. As the crop progressed, the incident waves interacted more with the top canopy layer, resulting in dominant surface scattering. Consequently, we observed an increase in P_s to 45.98% during this period. The scattering power components derived from descending orbit RCM images exhibited dominant surface scattering. Accordingly, we observed P_s power to be 45.73% on 30 July and 45.51% on 15 August, respectively.

Over corn fields, the CPS on 1 July exhibited characteristics similarity to a horizontal dipole. We observed a mixture of odd-bounce ($P_s = 24.91\%$) and even-bounce ($P_d = 34.53\%$) scattering from corn fields during this period (Table VII). It is important to note that the combination of these two scattering mechanisms results in scattering similar to a horizontal dipole. This observation may be attributed to the interaction of the incident waves with the underlying ground and the small stems of the crop during the initial growth stages.

As the corn crop advanced, we observed the dominance of $P_v = 49.19\%$, indicating random scattering from the crop's canopy during 30 July and 27 August (Table VII). One can also note significant surface scattering from the corn crops during this period. The observation aligns with the limited penetration of incident C-band waves, primarily interacting with the broad corn leaves, resulting in surface scattering. Similarly, the scattering power components derived from descending orbit RCM images indicated dominant $P_v = 48.31\%$ and $P_s = 46.80\%$ power on 30 July and 15 August, respectively.

For cereal crops on 1 July, the dominant scattering was characterized by $P_v = 47.59\%$ (Table VII). This suggests the prevalence of random scattering from the crop, particularly during the heading to the flowering stage. As the crop progressed to the fruit development stage on 30 July, $P_s = 51.87\%$ became dominant, signifying interaction mainly with the top canopy layer and resulting in surface scattering. At the senescence stage, extended interaction of incident waves with crop canopy layers caused an increase in P_v to 41.87%.

Nevertheless, the scattering powers derived from the descending orbit RCM image resulted in dominant random scattering ($P_v = 57.45\%$) on 30 July. In the descending pass, the incident waves possibly interacted more with the crop canopy, leading to diffusion and random scattering. Further, during 15 August, we found the P_s power to increase to 48.78% (Table VII). This increase suggests more interaction of the incident waves with the ground surface during the ripening stage.

D. Classification Results

Finally, the classification results obtained from the two defined scenarios are presented. The evaluation of image classification accuracy involves comparing the classification results with actual measurements. This study employs widely used metrics, such as precision, recall, F1-score, and overall accuracy (OA) to assess the classification results in different scenarios. In addition, z-score values are utilized to indicate the significance of each feature in the classification process.

1) Scenario-1 (S1) Accuracy Assessment: In the first scenario, the supervised RF classification method was employed, utilizing two different feature sets in separate runs: the combination of RCM intensity channels and $m - \chi$ components and the combination of RCM intensity channels and $\mu - \chi$ components. The same training areas were employed to generate classification results for both feature sets. A total of 275 individual polygon areas representing soybean, hay, cereal, and corn classes were selected from the available reference data for training the machine learning classifier. The classification accuracy of Scenario 1 (S1) is shown in Fig. 13, and detailed results are presented in Table VIII. These decomposition techniques were compared to assess improvements in land cover classification. Notably, in the results obtained from S1, one significant misclassification was observed where cereal areas were inaccurately classified as corn. This misclassification was more pronounced when using the $m - \chi$ decomposition method.

2) Scenario-2 (S2) Accuracy Assessment: In the second scenario, maps were generated by combining all the features listed earlier (refer to Table II) for both single-date and multi-date RCM images. When considering a single-date image, Scenario 2 (S2) demonstrated superior classification performance compared with S1, achieving an OA of 80.51% (Fig. 14(a) and Table IX). It demonstrated commendable capability in distinguishing between the hay and cereal crop areas. However, it should be noted that not all crop types could be accurately classified using a single-date feature combination. This scenario illustrates the optimal accuracy achievable with a single-date RCM image in our study.

Across all cases, multi-date crop mapping in S2 demonstrated a significant improvement in classification accuracy. As shown in Fig. 14(b) and detailed in Table IX, the results obtained using multitemporal features in S2 achieved a high OA of 89.71%. This represents the highest classification accuracy for each crop type, benefiting from a relatively large dataset as input.

The superior performance of S2 can be attributed to the generalization of data, reducing the impact of noise. Moreover, it underscores the importance of feature extraction during different phenological stages of crop cycles, contributing to enhanced crop classification results. Notably, the two dominant crop types, soybean and corn, were consistently the most accurately predicted classes overall in both scenarios, likely due to a relatively larger number of training samples for these two groups.

Our exploration of crop classification using multi-date images especially included examining the potential impact of chronological order on OA. Our results suggest that the order of predictors, i.e., polarimetric parameters derived from time series SAR datasets, does not introduce significant bias in classification accuracy. This chronological independence can be attributed to the design of the RF algorithm. Each tree in the ensemble is constructed from a random subset of the input features, introducing feature randomization. This ensures temporal independence, and consequently, any change in the order of input parameters does not adversely affect the accuracy of the model.

3) Feature Importance for Crop Classification: The RF classifier offers a significant advantage in evaluating input variables and determining their importance and contribution to classification accuracy. In the context of all input features and four land cover classes, the S2 scenario utilized RF-computed predictor importance values to assess the significance of features.

Fig. 15 presents the normalized average importance of all input variables, revealing the overall contribution of features. Through statistical analysis, it becomes evident that the P_v component of the $\mu - \chi$ method emerges as the most crucial input variable influencing the accuracy of crop mapping. Following closely, the volumetric component of the $m - \chi$ decomposition stands out as the next most significant factor. This prominence

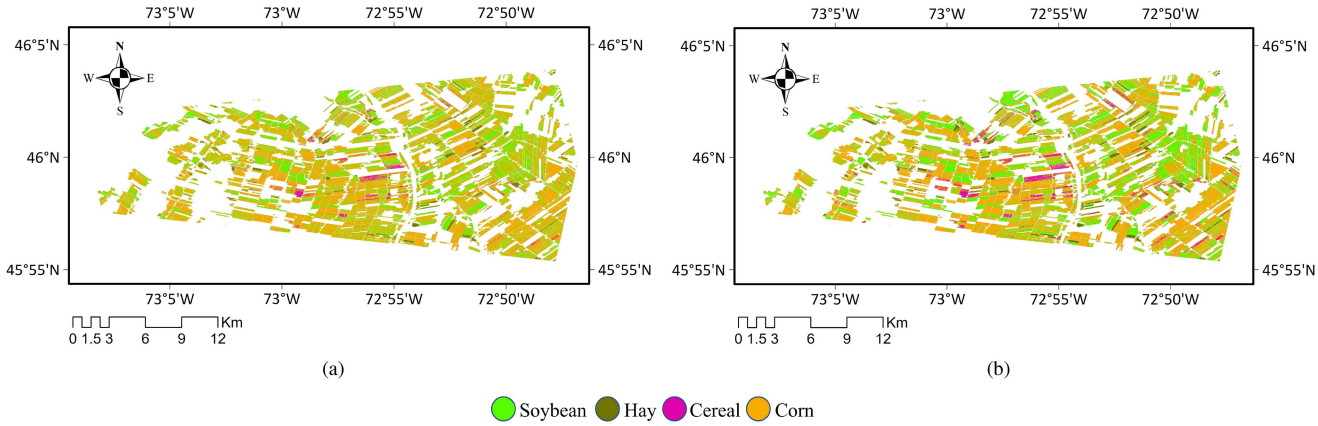

Fig. 13. Best classification maps obtained in S1 using the combination of (a) $m-\chi$ features and (b) $\mu-\chi$ features.

TABLE VIII
CROP GROUPS DISCRIMINATION ACCURACY ASSESSMENT BASED ON SINGLE-DATE IMAGERY IN S1

Acquisition Date	Estimator	$m-\chi$					$\mu-\chi$				
		Soybean	Hay	Cereal	Corn	Overall	Soybean	Hay	Cereal	Corn	Overall
Ascending 2021-07-01	Precision	0.60	0.50	0.30	0.70	0.52	0.65	0.60	0.35	0.75	0.58
	Recall	0.55	0.70	0.60	0.65	0.62	0.60	0.65	0.50	0.70	0.62
	F1-score	0.57	0.60	0.45	0.68	0.57	0.62	0.62	0.42	0.72	0.60
	Accuracy					69.2%					67.44%
Ascending 2021-07-30	Precision	0.55	0.48	0.22	0.72	0.52	0.67	0.62	0.4	0.86	0.64
	Recall	0.50	0.62	0.50	0.58	0.56	0.74	0.85	0.86	0.73	0.8
	F1-score	0.52	0.55	0.35	0.65	0.54	0.7	0.72	0.55	0.79	0.69
	Accuracy					67.51%					74.46%
Ascending 2021-08-27	Precision	0.58	0.52	0.25	0.75	0.55	0.70	0.68	0.38	0.80	0.62
	Recall	0.50	0.65	0.55	0.60	0.58	0.55	0.60	0.45	0.65	0.58
	F1-score	0.54	0.58	0.40	0.67	0.54	0.62	0.64	0.33	0.72	0.58
	Accuracy					63.4%					69.34%
Descending 2021-07-30	Precision	0.51	0.44	0.18	0.80	0.48	0.68	0.65	0.30	0.78	0.6
	Recall	0.61	0.75	0.68	0.63	0.67	0.62	0.68	0.45	0.7	0.62
	F1-score	0.56	0.55	0.29	0.71	0.53	0.65	0.66	0.36	0.74	0.61
	Accuracy					63.12%					73.28%
Descending 2021-08-15	Precision	0.58	0.50	0.28	0.75	0.53	0.62	0.55	0.35	0.68	0.58
	Recall	0.62	0.68	0.48	0.72	0.65	0.58	0.72	0.65	0.70	0.66
	F1-score	0.60	0.58	0.36	0.74	0.58	0.60	0.63	0.44	0.69	0.60
	Accuracy					65.14%					71.5%

TABLE IX
CROP GROUPS DISCRIMINATION ACCURACY ASSESSMENT USING S2

Acquisition Date	Method	Estimator	Soybean	Hay	Cereal	Corn	Overall
Ascending 2021-07-30	Single-date	Precision	0.75	0.72	0.54	0.89	0.73
		Recall	0.80	0.91	0.92	0.79	0.86
		F1-score	0.77	0.81	0.68	0.84	0.77
		Accuracy					80.51%
Five RCM images time-series	Multi-date	Precision	0.89	0.87	0.82	0.92	0.88
		Recall	0.89	0.91	0.87	0.91	0.90
		F1-score	0.89	0.89	0.84	0.92	0.89
		Accuracy					89.71%

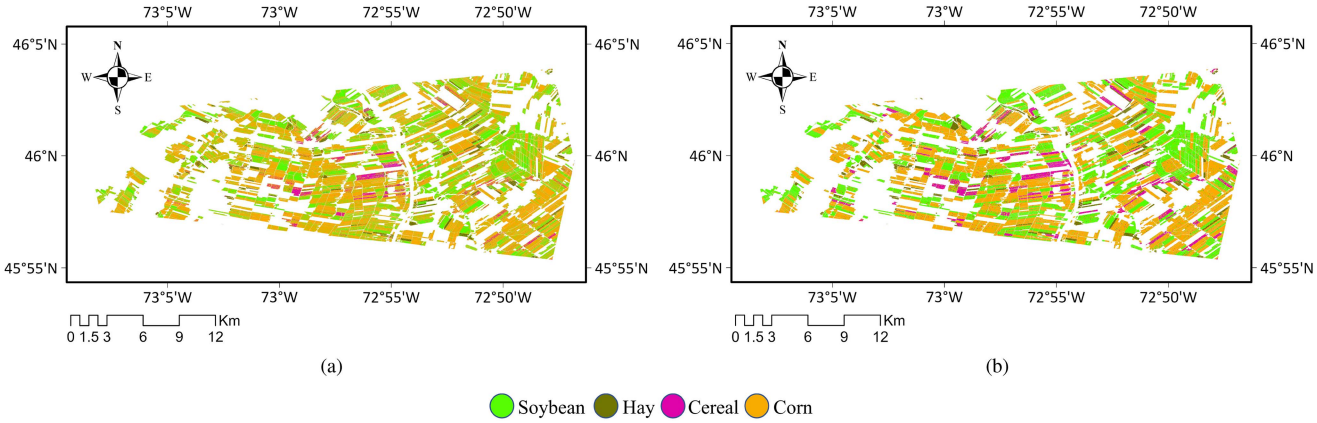

Fig. 14. Comparative evaluation of classification results based on S2. (a) Single-date. (b) Multi-Date.

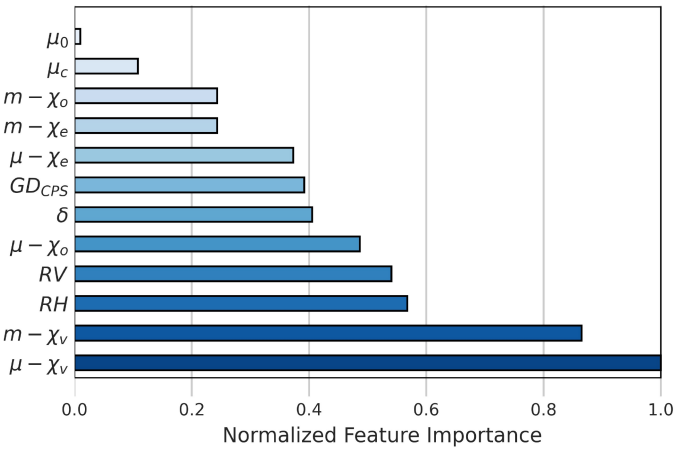

Fig. 15. Feature importance ranking obtained in S2.

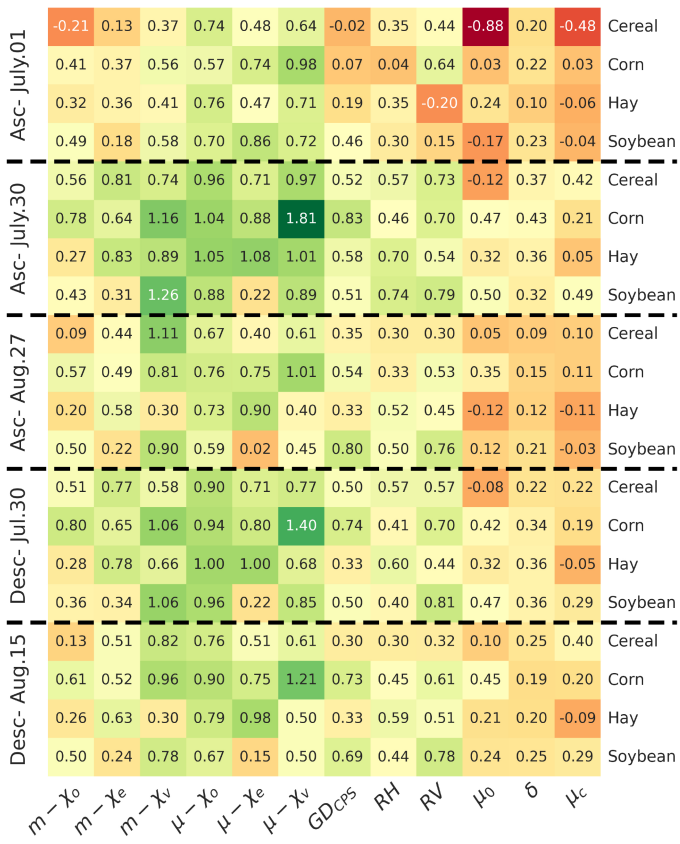

Fig. 16. z-score chart for the four crop classes of interest. Colors, ranging along the red to green gradient, represent the importance level of features, with red indicating lower influence and green reflecting higher influence. The horizontal and vertical axes of the z-score chart represent the feature and time domains, respectively.

can be attributed to the fact that volumetric scattering components dominate vegetation canopy interactions.

The RF classifier's evaluation of input variables reveals the importance of different features in the classification process. In this context, the RH intensity channel of RCM data demonstrates comparable significance to the RV intensity channel. Meanwhile, three parameters, P_s, δ, and $\mathrm{GD_{CPS}}$, portray lower importance than the intensity channels but still contribute effectively to the classification. Notably, the μ_c parameter holds a higher importance value than μ_0 in this analysis.

4) z-Score Values: We utilized the z-score values to provide an objective measure for an integrative assessment. This approach indicates the distance and direction of a variable's deviation from the average value of the distribution, expressed in terms of the standard deviation. Higher z-score values suggest a more significant impact on evaluation performance. As shown in Fig. 16, $\mu - \chi_\mathrm{v}$ and $m - \chi_\mathrm{v}$ exhibit the highest z-score values among all variables when dominant crops (e.g., corn) reach the mature stage. Intensity channels also proved effective in crop classification. In addition, the $\mathrm{GD_{CPS}}$ descriptor demonstrated relevance during both green and yellow leaves periods.

Statistical significance testing of per-pixel classification accuracy results using the z-score revealed that integrated feature sets comprising $\mu - \chi$ and $m - \chi$ powers outperformed all other tested input features. In summary, the effectiveness ranking of the employed features is as follows: $\mu - \chi$ components $>$ $m - \chi$ components $>$ intensity channels $>$ $\mathrm{GD_{CPS}}$ $>$ wave descriptors.

V. Conclusion

The study introduced three descriptors, CPS, DCPS, and GD, to analyze the scattering behavior exhibited by four crop types (soybean, hay, cereal, and corn) throughout the growing season using five RCM images acquired in CP StripMap mode over a test site in Quebec, Canada, with two primary objectives: The characterization of crop-type scattering and crop discrimination.

The analysis of time-series CPS has yielded insightful observations. Notably, during the active season marked by evolving vegetation structures, the variations in scattered waves have unveiled distinct scattering mechanisms inherent to different crop types. This emphasizes the potential sensitivity of CPS to physical and structural changes in plants. Notably, the discernible differences in wave ellipticity and orientation angles at the maximum polarization point ($P_{\max}$) across these crops are noteworthy.

In particular, the polarization states and the concept of scattering purity (μ) for agricultural fields add an additional dimension to assessing the agricultural landscape. For instance, the polarization states of the incident waves tend to be preserved for soybean during the initial growth phase. In contrast, for hay and corn crops, this preservation of polarization states becomes more pronounced during the later stages of the growth cycle.

The DCPS descriptor provides complementary information to CPS analysis, offering insights into the dis/similarity between any consecutive two CPSs of a given crop type. It informs about changes in scattering patterns, aligning with variations or growth in the foliage of crop plants. For instance, in cereal fields, where random scattering is predominant from the heading to the flowering stage, the DCPS descriptor between acquisitions on 1 July and 30 July indicates the shift from random to surface scattering. Meanwhile, for soybean, the transition is from trihedral to vertical dipole scattering during the same period. In addition, the GD target discrimination descriptor, measuring dis/similarity between two CPSs across the study area, proves valuable in the context of crop classification.

This study extensively examined CP-SAR data, and diverse parameters were extracted for crop classification using the RF classifier. Multiple classification runs were conducted across two scenarios, testing various combinations of CP inputs. The multi-date crop mapping approach achieved an impressive OA of 89.71%, highlighting the effectiveness of integrating features from CP data. Notably, the random scattering component of the $\mu - \chi$ decomposition emerged as a critical feature. In addition, the GD descriptor demonstrated a relatively high level of importance in the classification process.

It is imperative to undergo rigorous validation and sensitivity assessments to enhance the operational agricultural crop characterization using SAR observations, particularly when dealing with multifrequency observations, especially at L-band. This strategic approach offers a unique opportunity to delve into the frequency-dependent behavior of croplands, considering varying penetration depths and responses to biophysical variables. Collecting field data for crop fields and capturing crucial phenological features, such as the percentage of canopy coverage and growth stage becomes indispensable. These assessments play a pivotal role in fortifying the reliability of proposed methods and contribute to developing more robust operational crop monitoring frameworks, thereby, shaping the trajectory of future studies in this domain.

Acknowledgment

The authors would like to express sincere gratitude to the Canadian Space Agency (CSA) for providing access to the RADARSAT Constellation Mission (RCM) dataset. The availability of this dataset played a pivotal role in conducting our research and substantially contributed to the quality of the results presented in this article. Finally, the authors would like to thank the Quebec Ministry of International Relations and Francophonie for partially funding this research through the 2020–2022's Quebec-Maharashtrra Cooperation Program.

References

[1] C. Atzberger, "Advances in remote sensing of agriculture: Context description, existing operational monitoring systems and major information needs," *Remote Sens.*, vol. 5, no. 2, pp. 949–981, 2013.

[2] A. Chakhar, D. O.-Terol, D. Hernández-López, R. Ballesteros, J. F. Ortega, and M. A. Moreno, "Assessing the accuracy of multiple classification algorithms for crop classification using Landsat-8 and Sentinel-2 data," *Remote Sens.*, vol. 12, no. 11, 2020, Art. no. 1735.

[3] J. A. V. Vliet and K. Giller, "Mineral nutrition of COCOA: A review," *Adv. Agronomy*, vol. 141, pp. 185–270, 2017.

[4] C. Lin, L. Zhong, X.-P. Song, J. Dong, D. B. Lobell, and Z. Jin, "Early-and in-season crop type mapping without current-year ground truth: Generating labels from historical information via a topology-based approach," *Remote Sens. Environ.*, vol. 274, 2022, Art. no. 112994.

[5] E. Benami et al., "Uniting remote sensing, crop modelling and economics for agricultural risk management," *Nature Rev. Earth Environ.*, vol. 2, no. 2, pp. 140–159, 2021.

[6] S. Dey, N. Bhogapurapu, S. Homayouni, A. Bhattacharya, and H. McNairn, "Unsupervised classification of crop growth stages with scattering parameters from dual-pol Sentinel-1 SAR data," *Remote Sens.*, vol. 13, no. 21, 2021, Art. no. 4412.

[7] M. Schmidt, M. Pringle, R. Devadas, R. Denham, and D. Tindall, "A framework for large-area mapping of past and present cropping activity using seasonal landsat images and time series metrics," *Remote Sens.*, vol. 8, no. 4, 2016, Art. no. 312.

[8] P. Singh et al., "Hyperspectral remote sensing in precision agriculture: Present status, challenges, and future trends," in *Hyperspectral Remote Sensing*. Amsterdam, The Netherlands: Elsevier, 2020, pp. 121–146.

[9] W. G. Bastiaanssen, D. J. Molden, and I. W. Makin, "Remote sensing for irrigated agriculture: Examples from research and possible applications," *Agricultural Water Manage.*, vol. 46, no. 2, pp. 137–155, 2000.

[10] L. Chong et al., "Mapping the fallowed area of paddy fields on Sanjiang plain of northeast China to assist water security assessments," *J. Integrative Agriculture*, vol. 19, no. 7, pp. 1885–1896, 2020.

[11] L. Meng et al., "Assessment of the effectiveness of spatiotemporal fusion of multi-source satellite images for cotton yield estimation," *Comput. Electron. Agriculture*, vol. 162, pp. 44–52, 2019.

[12] R. Nasirzadehdizaji, Z. Cakir, F. B. Sanli, S. Abdikan, A. Pepe, and F. Caló, "Sentinel-1 interferometric coherence and backscattering analysis for crop monitoring," *Comput. Electron. Agriculture*, vol. 185, 2021, Art. no. 106118.

[13] J. M. Peña, P. A. Gutiérrez, C. H.s-Martínez, J. Six, R. E. Plant, and F. L.-Granados, "Object-based image classification of summer crops with machine learning methods," *Remote Sens.*, vol. 6, no. 6, pp. 5019–5041, 2014.

[14] N. Kussul, M. Lavreniuk, S. Skakun, and A. Shelestov, "Deep learning classification of land cover and crop types using remote sensing data," *IEEE Geosci. Remote Sens. Lett.*, vol. 14, no. 5, pp. 778–782, May 2017.

[15] G. W. Gella, W. Bijker, and M. Belgiu, "Mapping crop types in complex farming areas using SAR imagery with dynamic time warping," *ISPRS J. Photogrammetry Remote Sens.*, vol. 175, pp. 171–183, 2021.

[16] J. Guo, P.-L. Wei, J. Liu, B. Jin, B.-F. Su, and Z.-S. Zhou, "Crop classification based on differential characteristics of h/α scattering parameters for multitemporal quad-and dual-polarization SAR images," *IEEE Trans. Geosci. Remote Sens.*, vol. 56, no. 10, pp. 6111–6123, Oct. 2018.

[17] S. Dey et al., "In-season crop classification using elements of the Kennaugh matrix derived from polarimetric RADARSAT-2 SAR data," *Int. J. Appl. Earth Observ. Geoinformation*, vol. 88, 2020, Art. no. 102059.

[18] D. Mandal, V. Kumar, A. Bhattacharya, Y. S. Rao, P. Siqueira, and S. Bera, "Sen4Rice: A processing chain for differentiating early and late transplanted rice using time-series Sentinel-1 SAR data with Google Earth engine," *IEEE Geosci. Remote Sens. Lett.*, vol. 15, no. 12, pp. 1947–1951, Dec. 2018.

[19] P. Ghosh, D. Mandal, S. Wilfling, J. Hollberg, D. Bargiel, and A. Bhattacharya, "Synergy of optical and synthetic aperture radar data for early-stage crop yield estimation: A case study over a state of Germany," *Geocarto Int.*, vol. 37, no. 25, pp. 10 743–10 766, 2022.

[20] D. Mandal and Y. Rao, "SASYA: An integrated framework for crop biophysical parameter retrieval and within-season crop yield prediction with SAR remote sensing data," *Remote Sens. Appl.: Soc. Environ.*, vol. 20, 2020, Art. no. 100366.

[21] D. Mandal, V. Kumar, H. McNairn, A. Bhattacharya, and Y. Rao, "Joint estimation of plant area index (PAI) and wet biomass in wheat and soybean from c-band polarimetric SAR data," *Int. J. Appl. Earth Observ. Geoinf.*, vol. 79, pp. 24–34, 2019.

[22] D. Mandal, V. Kumar, J. M. L.-Sanchez, A. Bhattacharya, H. McNairn, and Y. S. Rao, "Crop biophysical parameter retrieval from Sentinel-1 SAR data with a multi-target inversion of water cloud model," *Int. J. Remote Sens.*, vol. 41, no. 14, pp. 5503–5524, 2020.

[23] D. Mandal et al., "Assessment of rice growth conditions in a semi-arid region of India using the generalized radar vegetation index derived from RADARSAT-2 polarimetric SAR data," *Remote Sens. Environ.*, vol. 237, 2020, Art. no. 111561.

[24] P. Ferrazzoli, S. Paloscia, P. Pampaloni, G. Schiavon, D. Solimini, and P. Coppo, "Sensitivity of microwave measurements to vegetation biomass and soil moisture content: A case study," *IEEE Trans. Geosci. Remote Sens.*, vol. 30, no. 4, pp. 750–756, Jul. 1992.

[25] M. W. Davidson, T. L. Toan, F. Mattia, G. Satalino, T. Manninen, and M. Borgeaud, "On the characterization of agricultural soil roughness for radar remote sensing studies," *IEEE Trans. Geosci. Remote Sens.*, vol. 38, no. 2, pp. 630–640, Mar. 2000.

[26] M. Mahdianpari et al., "Mid-season crop classification using dual-, compact-, and full-polarization in preparation for the radarsat constellation mission (RCM)," *Remote Sens.*, vol. 11, no. 13, 2019, Art. no. 1582.

[27] M. Dabboor et al., "The RADARSAT constellation mission core applications: First results," *Remote Sens.*, vol. 14, no. 2, 2022, Art. no. 301.

[28] R. K. Raney, "Hybrid-polarity SAR architecture," *IEEE Trans. Geosci. Remote Sens.*, vol. 45, no. 11, pp. 3397–3404, Nov. 2007.

[29] L. D. Robertson, H. McNairn, X. Jiao, C. McNairn, and S. O. Ihuoma, "Monitoring crops using compact polarimetry and the RADARSAT constellation mission," *Can. J. Remote Sens.*, vol. 48, no. 6, pp. 793–813, 2022.

[30] M. Mahdianpari, B. Salehi, F. Mohammadimanesh, and B. Brisco, "An assessment of simulated compact polarimetric SAR data for wetland classification using random forest algorithm," *Can. J. Remote Sens.*, vol. 43, no. 5, pp. 468–484, 2017.

[31] F. Charbonneau et al., "Compact polarimetry overview and applications assessment," *Can. J. Remote Sens.*, vol. 36, no. sup2, pp. S298–S315, 2010.

[32] B. Brisco, K. Li, B. Tedford, F. Charbonneau, S. Yun, and K. Murnaghan, "Compact polarimetry assessment for rice and wetland mapping," *Int. J. Remote Sens.*, vol. 34, no. 6, pp. 1949–1964, 2013.

[33] L. Xie, H. Zhang, H. Li, and C. Wang, "A unified framework for crop classification in southern China using fully polarimetric, dual polarimetric, and compact polarimetric SAR data," *Int. J. Remote Sens.*, vol. 36, no. 14, pp. 3798–3818, 2015.

[34] V. Kumar, H. McNairn, A. Bhattacharya, and Y. S. Rao, "Temporal response of scattering from crops for transmitted ellipticity variation in simulated compact-pol SAR data," *IEEE J. Sel. Topics Appl. Earth Observ. Remote Sens.*, vol. 10, no. 12, pp. 5163–5174, Dec. 2017.

[35] J. D. B.-Berman and J. M. L.-Sanchez, "Time series of hybrid-polarity parameters over agricultural crops," *IEEE Geosci. Remote Sens. Lett.*, vol. 9, no. 1, pp. 139–143, Jan. 2012.

[36] S. R. Cloude, D. G. Goodenough, and H. Chen, "Compact decomposition theory," *IEEE Geosci. Remote Sens. Lett.*, vol. 9, no. 1, pp. 28–32, Jan. 2012.

[37] A. Verma, D. Haldar, and A. Bhattacharya, "Polarimetric signature analysis of various crop-types using multi-source dual-frequency SAR data," *Geocarto Int.*, vol. 37, no. 25, pp. 8860–8881, 2022.

[38] A. Verma, S. Dey, N. Bhogapurapu, C. L.-Martínez, and A. Bhattacharya, "Dual polarimetric SAR signature for human-made target characterization," in *Proc. IEEE Int. India Geosci. Remote Sens. Symp.*, 2021, pp. 520–523.

[39] A. Verma, S. Dey, C. L.-Martínez, and A. Bhattacharya, "Radar target scattering signature for earth observation," in *Proc. URSI Regional Conf. Radio Sci.*, 2022, pp. 1–4.

[40] D. Ratha, E. Pottier, A. Bhattacharya, and A. C. Frery, "A PolSAR scattering power factorization framework and novel roll-invariant parameter-based unsupervised classification scheme using a geodesic distance," *IEEE Trans. Geosci. Remote Sens.*, vol. 58, no. 5, pp. 3509–3525, May 2020.

[41] R. K. Raney, J. T. Cahill, G. W. Patterson, and D. B. J. Bussey, "The m-chi decomposition of hybrid dual-polarimetric radar data with application to lunar craters," *J. Geophysical Res.: Planets*, vol. 117, no. E12, 2012, Art. no. JE003986.

[42] A. Bhattacharya, S. De, A. Muhuri, M. Surendar, G. Venkataraman, and A. Das, "A new compact polarimetric SAR decomposition technique," *Remote Sens. Lett.*, vol. 6, no. 12, pp. 914–923, 2015.

[43] V. Kumar, D. Mandal, A. Bhattacharya, and Y. Rao, "Crop characterization using an improved scattering power decomposition technique for compact polarimetric SAR data," *Int. J. Appl. Earth Observ. Geoinf.*, vol. 88, 2020, Art. no. 102052.

[44] S. Dey, A. Bhattacharya, D. Ratha, D. Mandal, and A. C. Frery, "Target characterization and scattering power decomposition for full and compact polarimetric SAR data," *IEEE Trans. Geosci. Remote Sens.*, vol. 59, no. 5, pp. 3981–3998, May 2021.

[45] J. J. V. Zyl, H. A. Zebker, and C. Elachi, "Imaging radar polarization signatures: Theory and observation," *Radio Sci.*, vol. 22, no. 04, pp. 529–543, 1987.

[46] V. F. R.-Galiano, B. Ghimire, J. Rogan, M. C.-Olmo, and J. P. R.-Sanchez, "An assessment of the effectiveness of a random forest classifier for land-cover classification," *ISPRS J. Photogrammetry Remote Sens.*, vol. 67, pp. 93–104, 2012.

[47] M. Belgiu and O. Csillik, "Sentinel-2 cropland mapping using pixel-based and object-based time-weighted dynamic time warping analysis," *Remote Sens. Environ.*, vol. 204, pp. 509–523, Jan. 2018.

[48] Z. Akhavan, M. Hasanlou, M. Hosseini, and H. McNairn, "Decomposition-based soil moisture estimation using UAVSAR fully polarimetric images," *Agronomy*, vol. 11, no. 1, 2021, Art. no. 145.

[49] M. Mahdianpari et al., "A large-scale change monitoring of wetlands using time series landsat imagery on Google Earth engine: A case study in newfoundland," *GIScience Remote Sens.*, vol. 57, no. 8, pp. 1102–1124, 2020.

[50] D. Uppala, R. K. Venkata, S. Poloju, S. M. V. Rama, and V. K. Dadhwal, "Discrimination of maize crop with hybrid polarimetric RISAT1 data," *Int. J. Remote Sens.*, vol. 37, no. 11, pp. 2641–2652, 2016.

[51] S. Chirakkal, D. Haldar, and A. Misra, "Evaluation of hybrid polarimetric decomposition techniques for winter crop discrimination," *Prog. Electromagn. Res. M*, vol. 55, pp. 73–84, 2017.

[52] Z. Yang, K. Li, L. Liu, Y. Shao, B. Brisco, and W. Li, "Rice growth monitoring using simulated compact polarimetric C band SAR," *Radio Sci.*, vol. 49, no. 12, pp. 1300–1315, 2014.

[53] K. Dasari and A. Lokam, "Exploring the capability of compact polarimetry (hybrid pol) C band RISAT-1 data for land cover classification," *IEEE Access*, vol. 6, pp. 57 981–57 993, 2018.

[54] H. Jafarzadeh, A. Verma, M. Mahdianpari, E. W. Gill, A. Bhattacharya, and S. Homayouni, "Compact-polarimetric SAR signature analysis for wetland characterization using RADARSAT constellation mission," *IEEE Trans. Geosci. Remote Sens.*, vol. 62, 2024, Art. no. 5202016.

[55] L. D. Robertson et al., "Synthetic aperture radar (SAR) image processing for operational space-based agriculture mapping," *Int. J. Remote Sens.*, vol. 41, no. 18, pp. 7112–7144, 2020.

[56] Y. Zhu, X. Deng, and S. Newsam, "Fine-grained land use classification at the city scale using ground-level images," *IEEE Trans. Multimedia*, vol. 21, no. 7, pp. 1825–1838, Jul. 2019.

[57] L. Zhong, L. Hu, and H. Zhou, "Deep learning based multi-temporal crop classification," *Remote Sens. Environ.*, vol. 221, pp. 430–443, 2019.

[58] X.-P. Song et al., "National-scale soybean mapping and area estimation in the United States using medium resolution satellite imagery and field survey," *Remote Sens. Environ.*, vol. 190, pp. 383–395, 2017.

[59] A. Freeman and S. Durden, "A three-component scattering model for polarimetric SAR data," *IEEE Trans. Geosci. Remote Sens.*, vol. 36, no. 3, pp. 963–973, May 1998.

[60] Y. Yamaguchi, T. Moriyama, M. Ishido, and H. Yamada, "Four-component scattering model for polarimetric SAR image decomposition," *IEEE Trans. Geosci. Remote Sens.*, vol. 43, no. 8, pp. 1699–1706, Aug. 2005.

Hamid Jafarzadeh (Graduate Student Member, IEEE) received the B.Sc. degree in surveying and geomatics engineering from the University of Tabriz, Tabriz, Iran, in 2016, and the M.Sc. degree in remote sensing engineering from the School of Surveying and Geomatics Engineering, College of Engineering, University of Tehran, Tehran, Iran, in 2020. He is currently working toward the Ph.D. degree in electrical engineering with the Department of Engineering and Applied Science, Memorial University, St. John's, NL, Canada. His research interests include remote sensing and image processing; multispectral, hyperspectral, and PolSAR data analysis; machine learning; deep learning; and multisensor data classification in agroenvironmental applications, with a special focus on wetland mapping and characterization.

Mr. Jafarzadeh was a recipient of numerous awards and honors, including the Fellow of the School of Graduate Studies by the Memorial University and the Wally Read Best Young Professional Paper Award organized by IEEE Newfoundland Electrical and Computer Engineering Conference (NECEC) in 2023.

Abhinav Verma (Graduate Student Member, IEEE) received an integrated M.Tech degree in geoinformatics from the Central University of Jharkhand, Ranchi, India, in 2018. He is currently working toward the Ph.D. degree in geoinformatics and natural resources engineering with the Centre of Studies in Resources Engineering, Indian Institute of Technology Bombay (CSRE, IITB), Mumbai, India.

He was a Researcher with IIRS, ISRO, Dehradun. His research interest include advancing and applying radar remote sensing datasets for several land cover applications, including crop monitoring, built-up area mapping, wetland characterization, and change detection.

Mr. Verma was the recipient of the prestigious Prime Minister's Research Fellowship (PMRF) to pursue his doctoral degree.

Masoud Mahdianpari (Senior Member, IEEE) received the B.S. degree in surveying and geomatics engineering and the M.Sc. degree in remote sensing engineering from the School of Surveying and Geomatics Engineering, College of Engineering, University of Tehran, Tehran, Iran, in 2010 and 2013, respectively. He received the Ph.D. degree in electrical engineering from the Department of Engineering and Applied Science, Memorial University, St. John's, NL, Canada, in 2019.

In 2019, he was an Ocean Frontier Institute (OFI) Postdoctoral Fellow with Memorial University and C-CORE. He is currently a Remote Sensing Technical Lead with C-CORE and a Cross Appointed Professor with the Faculty of Engineering and Applied Science, Memorial University. He has authored or coauthored more than 150 publications, including peer-reviewed journal articles, conference papers, books, and book chapters. His research interests include remote sensing and image analysis, with a special focus on PolSAR image processing, multimodal data analytics, machine learning, geo big data, and deep learning.

Dr. Mahdianpari is also an Editorial Team Member for the *Remote Sensing Journal*, IEEE GEOSCIENCE AND REMOTE SENSING, the *Frontiers in Environmental Science Journal*, and the *Canadian Journal of Remote Sensing*. He was a recipient of the Research and Development Corporation Ocean Industries Student Research Award, organized by Newfoundland Industry and Innovation Center, amongst more than 400 submissions, in 2016, the T. David Collett Best Industry Paper Award organized by IEEE in 2016, the Com-Adv Devices, Inc., Scholarship for Innovation, Creativity, and Entrepreneurship from the Memorial University in 2017, the Artificial Intelligence for Earth Grant organized by Microsoft in 2018, and the Graduate Academic Excellence Award organized by Memorial University in 2019. In 2020, he received the Best Industry Paper Award organized by IEEE Newfoundland Electrical and Computer Engineering Conference (NECEC). In 2023, Dr. Mahdianpari achieved a global ranking in the top 1% of scientists, as reported by Stanford and Elsevier.

Avik Bhattacharya (Senior Member, IEEE) received the integrated M.Sc. degree in mathematics from the Indian Institute of Technology, Kharagpur, India, in 2000, and the Ph.D. degree in remote sensing image processing and analysis from Télécom ParisTech, Paris, France, and the Ariana Research Group, Institut National de Recherche en Informatique et en Automatique (INRIA), Sophia Antipolis, Nice, France, in 2007.

He is a Professor with the Centre of Studies in Resources Engineering, Indian Institute of Technology Bombay (CSRE, IITB), Mumbai, India. Before joining IITB, he was a Canadian Government Research Fellow with the Canadian Centre for Remote Sensing (CCRS) in Ottawa, ON, Canada. He received the Natural Sciences and Engineering Research Council of Canada Visiting Scientist Fellowship at the Canadian National Laboratories from 2008 to 2011.

His research interests include SAR polarimetry, statistical analysis of polarimetric SAR images, and applications of radar remote sensing in agriculture, cryosphere, urban, and planetary studies. He was the Associate Editor, and then, the Editor-in-Chief of IEEE GEOSCIENCE AND REMOTE SENSING LETTERS (GRSL) from 2019 to 2023. He has been the Guest Editor of the special issue on Applied Earth Observations and Remote Sensing in India in the IEEE JOURNAL OF SELECTED TOPICS IN APPLIED EARTH OBSERVATIONS AND REMOTE SENSING (J-STARS), 2017. He was one of the Guest Editors of the special stream on Advanced Statistical Techniques in SAR Image Processing and Analysis in IEEE GEOSCIENCE AND REMOTE SENSING LETTERS, 2018. He is the Founding Chairperson of the IEEE Geoscience and Remote Sensing Society (GRSS) Chapter of the Bombay Section. He leads the Microwave Remote Sensing Lab at CSRE, IITB.

Saeid Homayouni (Senior Member, IEEE) received the B.Sc. degree in surveying and geomatics engineering from the University of Isfahan, Isfahan, Iran, in 1996, the M.Sc. degree in remote sensing and geographic information systems from Tarbiat Modares University, Tehran, Iran, in 1999, and the Ph.D. degree in signal and image from Télécom Paris Tech, Paris, France, in 2005.

From 2006 to 2007, he was a Postdoctoral Fellow with the Signal and Image Laboratory, University of Bordeaux Agro-Science, Bordeaux, France. From 2008 to 2011, he was an Assistant Professor with the Department of Surveying and Geomatics, College of Engineering, University of Tehran, Tehran, Iran. From 2011 to 2013, through the Natural Sciences and Engineering Research Council of Canada Visitor Fellowship Program, he was with the Earth Observation Group of the Agriculture and Agri-Food Canada, Ottawa Center of Research and Development, Ottawa, ON, Canada. In 2013, he was a replacing Assistant Professor of remote sensing and geographic information systems with the Department of Geography, Environment, and Geomatics, University of Ottawa, Ottawa, ON, Canada. Since April 2019, he has been an Associate Professor of environmental remote sensing and geomatics with the Centre Eau Terre Environnement, Institut National de la Recherche Scientifique, Quebec, QC, Canada. He is currently leading a research group on Earth Observation Analytics by Artificial Intelligence. His research interests include optical and radar Earth observations analytics for urban and agroenvironmental applications.